International Journal of Rock Mechanics & Mining Sciences 158 (2022) 105168

Contents lists available at ScienceDirect

International Journal of Rock Mechanics and Mining Sciences

journal homepage: www.elsevier.com/locate/ijrmms

Identification of higher symmetry in triclinic stiffness tensor: Application to high pressure dependence of elastic anisotropy in deep underground structures

Ali Aminzadeh [a,*], Matěj Petružálek [a], Václav Vavryčuk [a,b], Tatiana I. Ivankina [c], Tomáš Svitek [a], Alice Petrlíková [d], Lubomír Staš [d], Tomáš Lokajíček [a]

[a] Institute of Geology of the Czech Academy of Sciences, Prague, Czech Republic
[b] Institute of Geophysics of the Czech Academy of Sciences, Prague, Czech Republic
[c] Frank Laboratory of Neutron Physics, Joint Institute for Nuclear Research, Dubna, Russia
[d] Institute of Geonics of the Czech Academy of Sciences, Czech Republic

ARTICLE INFO

Keywords:
Ultrasonic sounding
Dynamic elastic constants
Transverse isotropy
Orthorhombic/orthotropic symmetry
P waves
S waves

ABSTRACT

We present an approach of identifying anisotropy axes and the type of symmetry from ultrasonic measurements of 21 elastic constants of the complete stiffness tensor characterizing anisotropic materials. The approach is applied to examine anisotropic elasticity of two crystalline rock samples from two underground research laboratories: (1) the migmatized gneiss from Bukov in the Czech Republic; and (2) the Aare Granite from Grimsel in Switzerland. The full stiffness matrix is measured at selected pressure levels from 0.1 to 100 MPa. We demonstrate that the Bukov migmatized gneiss is orthorhombic, whereas the Grimsel granite is transversely isotropic under atmospheric pressure. The degree of anisotropy of both rocks decreases with applied confining pressure due to closing of preferentially oriented cracks. While the Grimsel granite is very sensitive to pressure and becomes almost isotropic at high pressures, a great portion of anisotropy in the Bukov migmatized gneiss remains even under high pressures due to its texture. The dependence of Young's and shear moduli with pressure emphasizes the importance of taking the pressure into account for underground projects.

1. Introduction

Most of rocks display elastic anisotropy, which is manifested by a directional dependence of propagation velocity of seismic waves.[1,2] Based on its origin, we distinguish between: (1) intrinsic anisotropy produced by the crystal preferred orientation or the shape preferred orientation,[3,4] and (2) extrinsic anisotropy, caused by the alignment of micro-cracks, cracks or fractures or by layering.[5,6] The propagation velocity and its anisotropy are influenced by in situ acting stress,[7] with two different phenomena being typically recognizable: (1) A characteristic rapid increase of velocity with pressure caused by microcrack closing. This effect is dominant at low pressure, typically below 100 MPa. It is accompanied by a decrease of degree of anisotropy, provided the cracks are preferentially aligned (e.g., Pros et al.[8]). (2) A linear increase of velocity with pressure observed after microcrack closing. The velocity increase is slow and anisotropy remains practically on the same level without any change in its orientation. This behavior is attributed to the pressure dependence of the elastic constants of a crack-free rock matrix.[8]

The most general type of anisotropy is associated with triclinic symmetry, which is described by 21 elastic parameters. However, the natural rock forming processes often result in anisotropy of higher symmetry related to a subparallel arrangement of rock constituents manifested, e.g., by foliation for metamorphic rocks and by aligned microcracks for igneous rocks. Such structures are conveniently described by transverse isotropy (TI) with five independent elastic constants and two angles describing the direction of the symmetry axis of anisotropy (hereinafter anisotropy axis). This anisotropy is very popular with many geophysical and geotechnical applications in practice.[9–14] While the applicability of TI is obvious, natural processes also often produce a more complex rock behavior such as anisotropy with orthorhombic symmetry (OS) or monoclinic symmetry (MS). Orthorhombic anisotropy can describe, e.g., effects of foliation and lineation in the foliation plane,[3] horizontal bedding with presence of aligned vertical cracks in fractured reservoirs,[15] mutually perpendicular

* Corresponding author.
E-mail address: aminzadeh@gli.cas.cz (A. Aminzadeh).

https://doi.org/10.1016/j.ijrmms.2022.105168
Received 7 January 2022; Received in revised form 17 April 2022; Accepted 11 July 2022

Nomenclature

c_{ijkl}, c^*_{ijkl} Stiffness tensor and its rotated form into the principal coordinate system
C_{IJ}, C^*_{IJ} The 6 x 6 stiffness matrix and its rotated form into the principal coordinate system
$E_i, i = 1,2,3$ Young's moduli along three orthogonal principal orientations of the material
$G_{ij}, i,j = 1,2,3$ Shear moduli in the plane ij
K_{MN}, $M, N = 1, \ldots,6$ The 6×6 transformation matrix
$\mathbf{n}, \mathbf{m}$ Unit vectors normal and within the symmetry plane
$\mathbf{x}, \mathbf{x}^*$ Vectors before and after rotation

Greek symbols
$\nu_{ij}, i,j = 1,2,3$ Poisson's ratios (the relative strain in direction j to the strain in direction i for a load applied in direction i)
$\Omega_{ij}, i,j = 1,2,3$ The 3×3 rotation matrix
δ_{ij} The 3×3 identity matrix

Abbreviations
BUK Bukov migmatized gneiss
GRM Grimsel granite
TI Transverse isotropy
OS Orthorhombic symmetry
URL Underground Research Laboratory

microcrack systems[16,17] or the presence of triaxial stress in an isotropic rock.[7,18] The OS is defined by 9 independent elastic constants and by three angles required to orient the principal mutually orthogonal directions with respect to an arbitrary coordinate system. Monoclinic symmetry is produced, e.g., by two non-orthogonal systems of fractures or even by a single system of microcorrugated fractures.[19]

Anisotropic constants are commonly estimated from P- and S-wave velocities, measured in the lab by the pulse–transmission method.[20] If anisotropy axes are known, e.g., from macroscopically visible structural features, it is sufficient to measure three P-wave and two S-wave velocities to estimate the stiffness tensor of TI[21–23] and six P-wave and three S-wave velocities to estimate the stiffness tensor of OS.[24] If the system of anisotropy axes is not obvious, the P- and S-wave velocities must be measured in a net with dense directional coverage and inverted for the most general stiffness tensor with 21 elastic constants in an experimentally chosen coordinate system.[18,25,26] As a result, the obtained stiffness tensor contains the complete information about the material, but it does not provide the symmetry type and the elastic constants of the material in its symmetry planes. Obviously, this difficulty might complicate geophysical and geotechnical interpretations of measurements.

The problem of identifying the symmetry type of an anisotropic material defined by 21 elastic constants has been addressed by several authors.[27–36] For example, Backus[27] used the Maxwell multi-poles to identify the symmetry type of the material. This was not an easy theory,[28] thus other researchers tried to present it through examples to make it more understandable (e.g., Baerheim[29]). Zou et al.[30] developed this method by adding the concept of a mirror plane. Another method was proposed by Aristegui and Baste[31] who studied a composite with a known fibrous reinforcement direction. They selected an arbitrarily oriented observation coordinate system (defined by Euler angles) resulting in a stiffness tensor with 21 non-zero elements and tried to identify the symmetry type of the material and its elastic parameters from this tensor. Using the Christoffel equation, two functionals were constructed for various types of symmetries. Cowin and Mehrabadi[32] proposed a simple way to determine the symmetry type of the crystals. They introduced two symmetric tensors of the second rank and identified the symmetry type of the material using the eigenvectors of these tensors. Arts[33,34] tried to apply this method to experimental data and numerically obtained the best plane of symmetry by evaluating various directions around the three eigenvectors to find the best solution with the least error for each symmetry type. Arts[33] showed that using the average of these two sets of eigenvectors is a reasonable solution and gives more stable results than those obtained from the more complicated method proposed by Backus,[27] especially, when data are contaminated by high level of triclinic noise.

In this study, we present an analytical approach of identifying anisotropy axes and the type of symmetry from measurements of 21 elastic constants of the complete stiffness tensor using the method proposed by Cowin and Mehrabadi[32] and by Ting.[37] We use an innovative way to implement this method and provide a MATLAB code SYMMETRY applicable to experimental data containing general triclinic noise. The main advantages of this method are: (1) the method is straightforward and easily reproducible, (2) the stiffness tensor is directly rotated into its principal orientations without a necessity to rotate it into different symmetry types and to select the best solution, and (3) we do not need to calculate the Euler angles for rotating the stiffness tensor into the principal coordinate system. We apply this approach to examine anisotropic elasticity of crystalline rock samples from two underground research laboratories: (1) the migmatized gneiss from Bukov in the Czech Republic; and (2) the Aare Granite from Grimsel in Switzerland. We have specified the anisotropy axes on experimental plots of the velocity distribution to visualize the efficiency of this method. We prove that the tested rock samples are well described by elastic anisotropy with OS. Besides, the effects of pressure on the symmetry type of these two rocks are studied in the range of pressure levels from 0.1 to 100 MPa. The rock-structure relation and the influence of pressure on the degree (strength) of anisotropy and the orientation of anisotropy axes are studied and discussed for both rock samples.

2. Identification of type of anisotropy symmetry and its principal coordinate system

The stiffness tensor c_{ijkl} of general anisotropy is defined by 21 independent elastic parameters. However, if anisotropy is of higher symmetry, this number can be reduced and tensor c_{ijkl} simplified when expressed in the principal coordinate system related to the symmetry axes. Since 9 forms of c_{ijkl} represent all 32 classes of crystals[38] except for isotropy, 10 forms of c_{ijkl} categorize the whole range of the known symmetries in the stiffness tensor.[37,39] Nevertheless, the dominant anisotropy types for the rocks are mostly TI and OS described only by 7 and 12 independent parameters, respectively. Therefore, an important task of any study of elastic anisotropy of unknown symmetry is to analyze the full stiffness tensor of 21 elastic parameters measured in an arbitrary coordinate system and to identify possible anisotropy symmetries and their principal coordinate system. For simplicity, we use the Einstein notation in deriving the formulas; however, the most important results will be expressed in the matrix form.

A transformed form of the symmetric matrix will not change when the transformation is implemented with respect to the symmetry plane. So, if a material has a symmetry described by matrix $\mathbf{\Omega}$, we can use the Einstein summation convention to write[37]:

$$c_{ijkl} = \Omega_{ip}\Omega_{jq}\Omega_{kr}\Omega_{lt}c_{pqrt}, \tag{1}$$

where $\mathbf{\Omega}$ must satisfy the following equations:

$$\Omega_{ij} = \delta_{ij} - 2n_i n_j, \tag{2a}$$

$$n_i\Omega_{ij} = -n_j, \tag{2b}$$

$$m_i\Omega_{ij} = m_j. \tag{2c}$$

Here, $\mathbf{n}$ is the unit vector perpendicular to the plane of symmetry, while $\mathbf{m}$ is an arbitrary unit vector in the plane of symmetry, i.e., their scalar

product equals zero, $\mathbf{n}\cdot\mathbf{m} = 0$. Symbol $\boldsymbol{\delta}$ is the identity matrix. It is useful to remind that matrix $\boldsymbol{\Omega}$ is an orthogonal or rotational matrix which means $\boldsymbol{\Omega}^T = \boldsymbol{\Omega}^{-1}$, hence $\boldsymbol{\Omega}\boldsymbol{\Omega}^T = \boldsymbol{\Omega}^T\boldsymbol{\Omega} = \boldsymbol{\delta}$. Hence, if real vectors $\mathbf{n}$ and $\mathbf{m}$ are rotated into new vectors $\mathbf{n}^*$ and $\mathbf{m}^*$, the length of the vectors and the angles between them will not change because $(\mathbf{n}^*)^T\mathbf{m}^* = (\boldsymbol{\Omega}\mathbf{n})^T(\boldsymbol{\Omega}\mathbf{m}) = \mathbf{n}^T\boldsymbol{\Omega}^T\boldsymbol{\Omega}\mathbf{m} = \mathbf{n}^T\mathbf{m}$.[37] The relation between the matrix $\boldsymbol{\Omega}$ and Euler angles is presented in Appendix B.

Cowin and Mehrabadi[32] used Eqs (1) and (2) to extract the following four conditions necessary and sufficient for $\mathbf{n}$ to be the normal vector to a plane of symmetry:

$$c_{ijkk}n_j = \left(c_{pqtt}n_pn_q\right)n_i, \tag{3a}$$

$$c_{ilkl}n_k = \left(c_{pqrq}n_pn_r\right)n_i, \tag{3b}$$

$$c_{ijkl}n_jn_ln_k = \left(c_{pqrt}n_pn_qn_rn_t\right)n_i, \tag{3c}$$

$$c_{ijkl}m_jm_ln_k = \left(c_{pqrt}n_pm_qn_rm_t\right)n_i. \tag{3d}$$

Eq. (3) shows that $\mathbf{n}$ is a common eigenvector of four 3×3 matrices c_{ijkk}, c_{ilkl}, $c_{ijkl}n_jn_l$, and $c_{ijkl}m_jm_l$. A repeated subscript indicates a summation, thus the tensors c_{ijkk} and c_{ilkl} can be expanded as symmetric matrices $\mathbf{U}$ and $\mathbf{V}$ (in the Voigt notation):

$$\mathbf{U} = \begin{bmatrix} C_{11}+C_{12}+C_{13} & C_{16}+C_{26}+C_{36} & C_{15}+C_{25}+C_{35} \\ & C_{12}+C_{22}+C_{23} & C_{14}+C_{24}+C_{34} \\ & & C_{13}+C_{23}+C_{33} \end{bmatrix} \tag{4a}$$

$$\mathbf{V} = \begin{bmatrix} C_{11}+C_{55}+C_{66} & C_{16}+C_{26}+C_{45} & C_{15}+C_{35}+C_{46} \\ & C_{22}+C_{44}+C_{66} & C_{24}+C_{34}+C_{56} \\ & & C_{33}+C_{44}+C_{55} \end{bmatrix} \tag{4b}$$

where matrix C_{IJ} represents the two-index Voigt notation of the stiffness tensor c_{ijkl}, see Musgrave.[39]

For the evaluation of Eq. (3d), one needs to know vector $\mathbf{m}$, which is dependent on vector $\mathbf{n}$. Therefore, Ting[37] multiplied both sides of Eqs (3c) and (3d) by $\mathbf{m}$ and obtained the following simplified equations due to the properties of orthogonal matrices:

$$c_{ijkl}m_in_jn_kn_l = 0, \tag{5a}$$

$$c_{ijkl}m_im_jm_kn_l = 0. \tag{5b}$$

In other words, it can be concluded that a stiffness tensor has a symmetry plane *only if* vector $\mathbf{n}$ is an eigenvector of both c_{ijkk} and c_{ilkl} and satisfies Eq. (5) for any two vectors $\mathbf{m}^{(\xi)}, \xi = 1, 2$ in the plane of symmetry that do not make an angle $\pi/3$ (or its multiples) with each other. It should be reminded that vectors $\mathbf{n}$ and $\mathbf{m}$ are perpendicular to each other.

Here, we only consider four common symmetry types of the rock materials although all 10 symmetry types known in the crystals can be determined using this method. We assume isotropic, orthorhombic, transversely isotropic, or triclinic materials, which are most common in geophysical applications (see Table 1). For a detailed classification of material symmetries according to properties of matrices $\mathbf{U}$ and $\mathbf{V}$, we refer to Cowin and Mehrabadi.[32]

An additional constraint (4th column) is needed for distinguishing between: (1) isotropic and cubic symmetry, and (2) transversely isotropic and tetragonal symmetry. C^*_{KL} are the components of the 6 x 6 stiffness matrix in the principal coordinate system.

If the sets of the normal vectors to the planes of symmetry and their properties are known, the number of symmetry planes is determined from Table 1.

When three normal vectors $\mathbf{n}$ (the common sets of eigenvectors of matrices c_{ijkk} and c_{ilkl}) are calculated from Eq. (4), the matrix $\boldsymbol{\Omega}$, called the coordinate transformation matrix or the rotation matrix, will be a 3×3 matrix composed of these three normal vectors, which transforms an initial coordinate system to the principal coordinate system:

$$\mathbf{x}^* = \boldsymbol{\Omega}\mathbf{x}, \tag{6}$$

where $\mathbf{x}$ is any initial vector, and $\mathbf{x}^*$ is its corresponding transformed vector. According to the transformations laws,[37] the transformed tensor c^*_{ijks} is calculated as:

$$\mathbf{C}^* = \mathbf{K}\mathbf{C}\mathbf{K}^T, \tag{7}$$

where, the 6×6 transformation matrix $\mathbf{K}$ is defined by Auld[25] or Ting[34]:

$$\mathbf{K} = \begin{bmatrix} \Omega_{11}^2 & \Omega_{12}^2 & \Omega_{13}^2 & 2\Omega_{12}\Omega_{13} & 2\Omega_{13}\Omega_{11} & 2\Omega_{11}\Omega_{12} \\ \Omega_{21}^2 & \Omega_{22}^2 & \Omega_{23}^2 & 2\Omega_{22}\Omega_{23} & 2\Omega_{23}\Omega_{21} & 2\Omega_{21}\Omega_{22} \\ \Omega_{31}^2 & \Omega_{32}^2 & \Omega_{33}^2 & 2\Omega_{32}\Omega_{33} & 2\Omega_{33}\Omega_{31} & 2\Omega_{31}\Omega_{32} \\ \Omega_{21}\Omega_{31} & \Omega_{22}\Omega_{32} & \Omega_{23}\Omega_{33} & \Omega_{22}\Omega_{33}+\Omega_{23}\Omega_{32} & \Omega_{23}\Omega_{31}+\Omega_{21}\Omega_{33} & \Omega_{21}\Omega_{32}+\Omega_{22}\Omega_{31} \\ \Omega_{31}\Omega_{11} & \Omega_{32}\Omega_{12} & \Omega_{33}\Omega_{13} & \Omega_{32}\Omega_{13}+\Omega_{33}\Omega_{12} & \Omega_{33}\Omega_{11}+\Omega_{31}\Omega_{13} & \Omega_{31}\Omega_{12}+\Omega_{32}\Omega_{11} \\ \Omega_{11}\Omega_{21} & \Omega_{12}\Omega_{22} & \Omega_{13}\Omega_{23} & \Omega_{12}\Omega_{23}+\Omega_{13}\Omega_{22} & \Omega_{13}\Omega_{21}+\Omega_{11}\Omega_{23} & \Omega_{11}\Omega_{22}+\Omega_{12}\Omega_{21} \end{bmatrix}. \tag{8}$$

Table 1
Determination of the type of symmetry in rock materials based on Eqs (4) and (5), adapted from Cowin and Mehrabadi.[32].

Symmetry type	Three eigenvalues (Eq. (4a) or Eq. (4b))	Number of eigenvectors satisfying Eq. (5)	Additional constraint
Isotropic	Three are equal	3	$C^*_{11} - C^*_{12} = 2C^*_{66}$
Transversely isotropic	Two are equal	3	$C^*_{11} - C^*_{12} = 2C^*_{66}$
Orthorhombic	Three are different	3	
Triclinic	Three are different	0	

In summary, the eigenvectors of matrices $\mathbf{U}$ and $\mathbf{V}$ identify the principal orientations of the material, whereas their eigenvalues inform us about the stiffness as well as the anisotropy degree of the material. For example, an isotropic rock has three equal eigenvalues, which are higher than those for a softer isotropic rock. Besides, a higher difference between two eigenvalues in an anisotropic rock reveals its higher ratio of anisotropy between those two directions.

An example of evaluating an ideal orthorhombic tensor in an arbitrary coordinate system and its transformation into the principal coordinate system is shown in Appendix A. In the case of an experimentally obtained stiffness matrix, we used a mean value of the two sets of eigenvectors obtained from Eqs. (4a) and (4b). The resultant 3×3 matrix was used as the coordinate transformation matrix $\boldsymbol{\Omega}$ and the 6×6

transformation matrix **K** was obtained using Eq. (8). The initial stiffness matrix was rotated into its principal directions using Eq. (7). Then, we investigated each of the three eigenvectors in matrix **Ω** to determine, whether it satisfies the conditions to be normal to a symmetry plane, see Eqs. (5a) and (5b). If all three eigenvectors have high residuals, the rock sample has less than three planes of symmetry. Otherwise, the sample is isotropic, transversely isotropic or orthorhombic. The sample is isotropic if all eigenvalues are almost equal, while it is transversely isotropic if only two eigenvalues are equal. Otherwise, the sample is orthorhombic. We have also shown the procedure of finding the symmetry type of the stiffness matrix contaminated by noise and the elastic parameters in the principal coordinate system in the supplementary MATLAB code SYMMETRY.

3. The rock samples

We analyzed elastic anisotropy of two rock samples from the underground research laboratories (URL) that are focused mainly on the investigation of functionality of deep repositories: (1) the BUK sample – migmatized gneiss, typical for the test site of the URL Bukov, Czech Republic; (2) the GRM sample - Central Aare granite, a predominant host rock of the URL Grimsel, Switzerland.

The Bukov URL is a part of the national program of the Radioactive Waste Authority of the Czech Republic (SURAO) for the siting process of a deep geological repository. The URL is located within the Moldanubian Unit of the Bohemian Massif, 550 m under the surface on level 12 of the former uranium mine Rožná, Czech Republic. The pressure at depth 550 m, caused by the overburden rock with an average density ~2.75 g/cm,[3] is about ~15 MPa. The horizontal stress ratio is ~2, with SHmax in the range of 25–35 MPa in the NE-SW direction.[40] The characteristic rocks are paragneiss, amphibolite, and migmatite. Their original foliation is related to the preferential orientation of biotite, amphibole, and orthoclase. It had been steeply dipping to the N–S direction and was at most places intensively refolded.[40,41] The BUK sample is fine to medium grained migmatized paragneiss that comes from level 22 (depth 1100 m) of Rožná mine and is practically identical with the host rock of the URL, 600 m above this level. It has a characteristic macroscopically visible foliation formed by alternating layers of leucosome and mesosome (Fig. 1a). The leucosome consists of varying proportions of quartz, plagioclase, and K-feldspar. The mesosome contains mainly biotite flakes, with a preferential orientation subparallel to the foliation (Fig. 1c). The biotite content is 20–30%.[41] Microcracks with a preferential orientation are mainly within the biotite and parallel to its basal planes (Fig. 1c). Based on the texture, we expect some of the grains boundaries to be sub-parallel with the foliation as well. The texture-related anisotropy of the migmatized gneiss was reported in Berčáková et al.[42] and Bukovská et al.[41] Petružálek et al.[43] described the texture related micro/macro scale-fracturing for Rožná migmatite using acoustic emissions.

The Grimsel URL is located at the 450 m depth within the Aare massif (Switzerland), on the border between the Central Aare granite and the Grimsel granodiorite. Both rocks present a macroscopically visible foliation, steeply dipping to the E–W direction, with a variable intensity generally increasing towards the mylonitic shear zones.[44] A more detailed geological/structural description of the Aare massif can be found in Wehrens et al.,[45] and the URL test site is described in Keusen et al.[46] The overburden pressure is ~12 MPa, considering the rock density of 2.7 g/cm^3. The far-field principal stresses are in the range: σ_1 = 13.1–14.4 MPa, σ_2 = 9.2–10.2 MPa, σ_3 = 8.6–9.7 MPa with σ_1 plunging to the east at 30–40°.[11] The Central Aare granite sample GRM comes from the over-coring at the drill hole LASMO 14-2. It is a slightly foliated leucocratic biotite meta-granite with a weakly porhyritic texture (plagioclase grains ~ 10 mm). Above 90% of the rock matrix is formed from quartz, feldspar, and plagioclase with addition of 4–8% of biotite. A weakly developed foliation is caused by alignment of biotite and flattening of interstitial quartz grains (Fig. 1b,d). Larger microcracks are parallel with the grain boundaries, especially between quartz and feldspars (Fig. 1d). The heavily sericitized feldspars contain a dense net of small microcracks. Table 1 in Krietsch et al.[11] lists the geology related works and their outputs performed at the URL up to 2017. Wenning et al.[44] described seismic anisotropy of the Grimsel granodiorite and its dependence on strength of the foliation and acting pressure. Nejati et al.[47] and Dambly et al.[48] estimated the texture-based transverse isotropy model to describe the static and dynamic anisotropy of the Aare granite. Krietsch et al.[11] applied a transverse isotropy model to improve the estimation of in situ stress tensor from overcoring strain measurements.

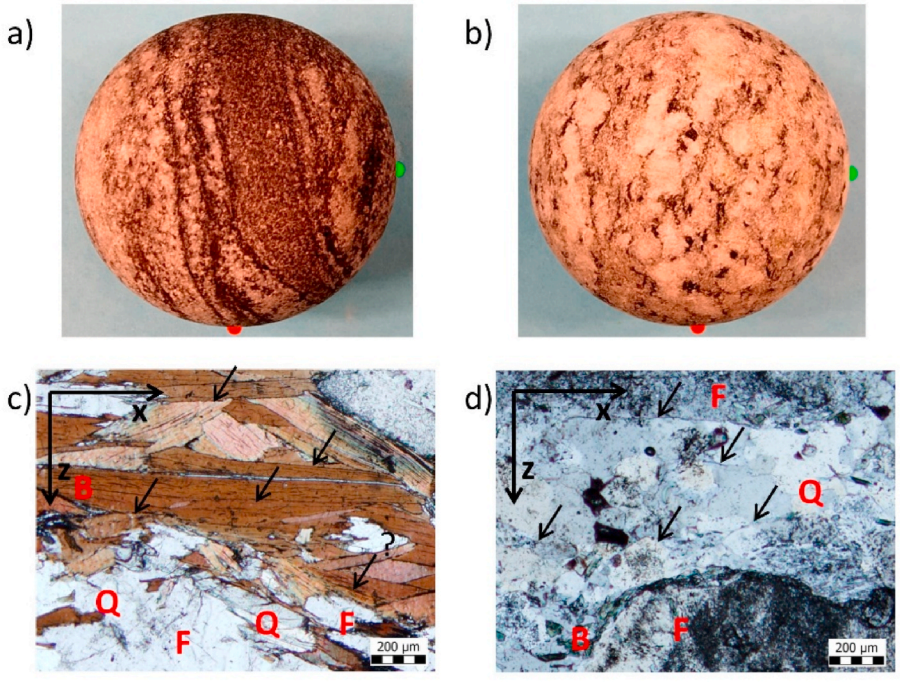

Fig. 1. Tested spherical samples in the experimental coordinate system: (a) BUK, the migmatized gneiss with a macroscopically visible foliation in the N–S direction, (b) GRM the Aare granite, with a weak foliation in the N–S direction. (c) thin section of migmatized gneiss (BUK) under plane polarized light. (d) thin section of the Aare granite (GRM) under plane polarized light. The *z*-axis is perpendicular to the foliation, the *x*-axis is parallel to the lineation. B – biotite, F- feldspar, Q – quartz. The short arrows point to the cracks subparallel to the foliation.

4. Experiments

The pressure dependent seismic anisotropy was measured by an apparatus originally proposed by Pros and Babuška,[49] who developed the pressure vessel for the measurements of the P-wave velocity anisotropy on spherical specimens in the 15° regular net of meridians and parallels (132 independent directions). Lokajícek and Svitek[50] designed a new high-pressure measuring head that allowed us to include the measurement of the shear-wave velocity in two mutually perpendicular polarizations. Here, the pulse transmission technique is applied to measure all the velocities across the 50 mm spherical sample in a regular net with 132 independent directions. The spherical samples were coated by a thin (0.1 mm) epoxy resin layer to prevent saturation of pore space of rock by the confining fluid. Shear-wave gel was used to improve the contact conditions between ultrasonic sensors and surface of the samples. Thanks to the point contact between flat ultrasonic sensors and the spherical surface of the sample, the ray (group) velocities are measured. The signals are pre-amplified by low noise 20 dB amplifier with a flat bandwidth in the range of 10 kHz–30 MHz. After 8 times averaging, the waveforms are registered with 100 MHz sampling frequency and the resolution of 10-bit dynamic range. The waveforms, and their dependence on the orientation and pressure, are similar to those published for the same experiment performed on anisotropic biotite gneiss.[25,51]

Klíma and Červený[52] introduced a numerical method for obtaining a full tensor of 21 elastic constants from the experimentally measured velocities. However, only 15 P-wave related constants were retrieved reliably if the S-wave velocities were not included into the inversion. Utilizing a recently developed measuring head allowed us to obtain also the S1 (faster) and S2 (slower) shear-wave velocity distributions and thus to retrieve a complete elastic tensor accurately.[25] We stress out that the S1 and S2 describe the faster and slower shear waves for each particular direction and are not directly related to their polarization. Hence, the polarization can flip in some cases (e.g., close to the shear wave singularities, see Vavrycuk[50]). Since we measure the ray (group) velocities but not the phase velocities, we have to recalculate the group velocities to the phase velocities before applying the inversion procedure. Therefore, we construct the wave surface from a dense grid of

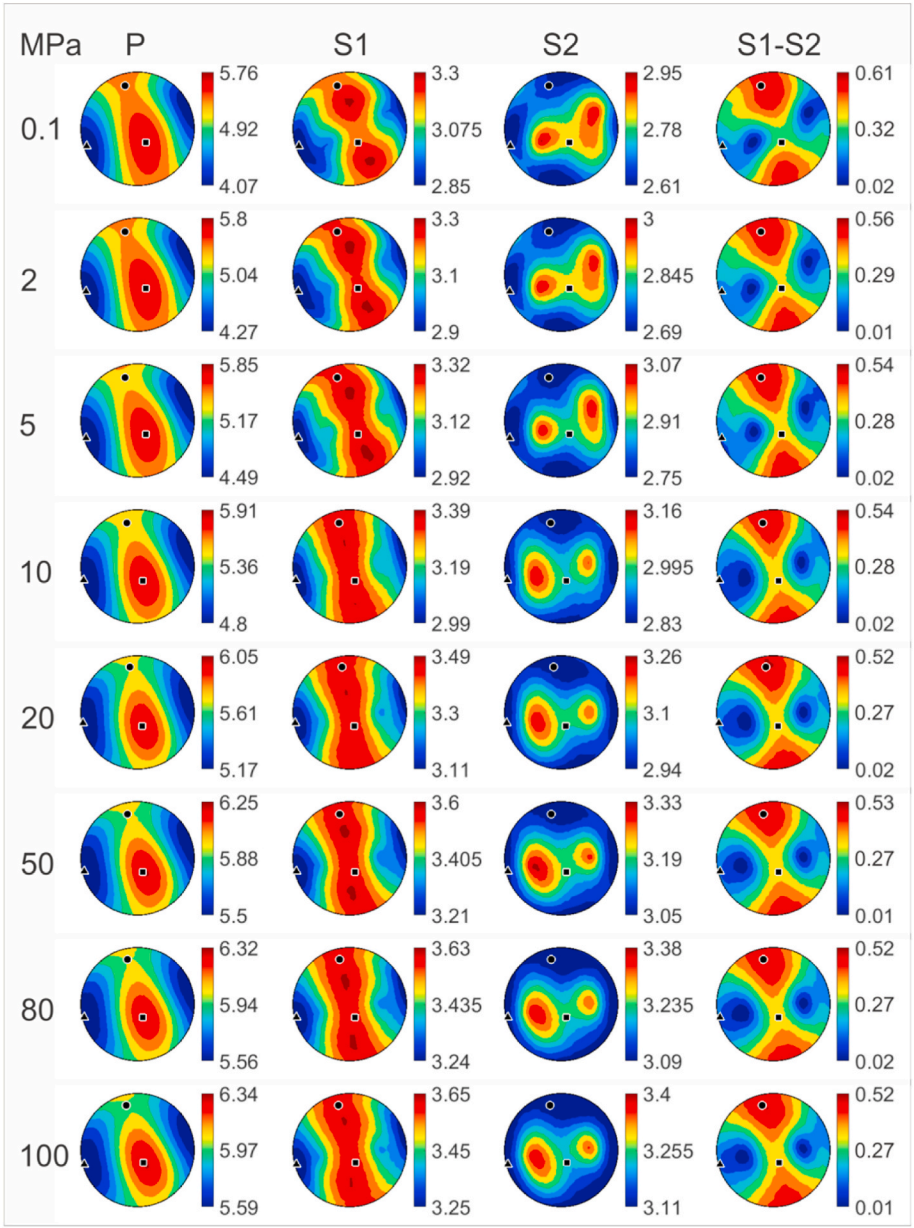

Fig. 2. The phase velocity distribution of the BUK sample plotted in the equal-area stereographic projection on the lower hemisphere. From left to right: velocities of the P, S1, S2 waves and the difference between the S1 and S2 velocities (in km/s). The pressure level increases from top to bottom. Stiffness tensor orientation is represented by the black symbols: square – x_1-axis (maximum P-wave velocity), circle – x_2-axis (intermediate P-wave velocity), triangle - x_3-axis (minimum P-wave velocity).

measured group velocities and by applying a simple transformation we obtain the corresponding phase velocity surface. The phase velocities are then inverted for a full set of anisotropic constants. The whole inversion process is described step by step in Svitek et al.[25]

Spherical specimens with a diameter of 50 mm were prepared from the BUK and GRM samples. They were vacuum dried at temperature 50 °C and covered by a 0.1 mm thick layer of epoxy resin, to isolate the rock from the pressurizing oil. The ultrasonic sounding was performed at selected levels of hydrostatic pressure: 0,1; 2; 5; 10; 20; 50 and 100 MPa for the BUK sample, and 0,1; 5; 10; 15; 20; 50; 80 and 100 MPa for the GRM sample. Three ultrasonic sensor pairs (P, S1, S2) were applied to generate and capture the corresponding ultrasonic waves. The rotation of the spherical sample and sensor holders allowed to measure the P, S1, and S2 velocities in 132 independent directions Lokajícek and Svitek.[50] The onsets of the firstly arriving P waves were picked automatically.[53] Due to the waveforms complexity at later times, a careful inspection was needed to manually determine the S1 and S2 arrivals. The phase velocities that are presented in the paper were obtained from the measured ray velocities according to Svitek et al.[25] The set of 3 x 132 phase velocities (P, S1, and S2) was used to retrieve the full stiffness tensor with 21 elastic constants.[25]

The P-, S1- and S2-phase velocity distributions are plotted for all pressure levels in Fig. 2 (BUK) and Fig. 3 (GRM). Both rocks display a similar relation between their texture and the P-wave velocity distribution. The high-velocity plane is parallel to the foliation, while the minimum velocity region is practically perpendicular to the foliation. A clearly visible maximum in the high-velocity plane does not change with pressure for the BUK sample, but slight changes are observed for the GRM sample above the 20 MPa pressure. Since all three extreme velocity directions (maximum, mean, and minimum) are practically mutually perpendicular, the application of the orthorhombic symmetry (OS) should be sufficient to characterize the anisotropic elasticity of both

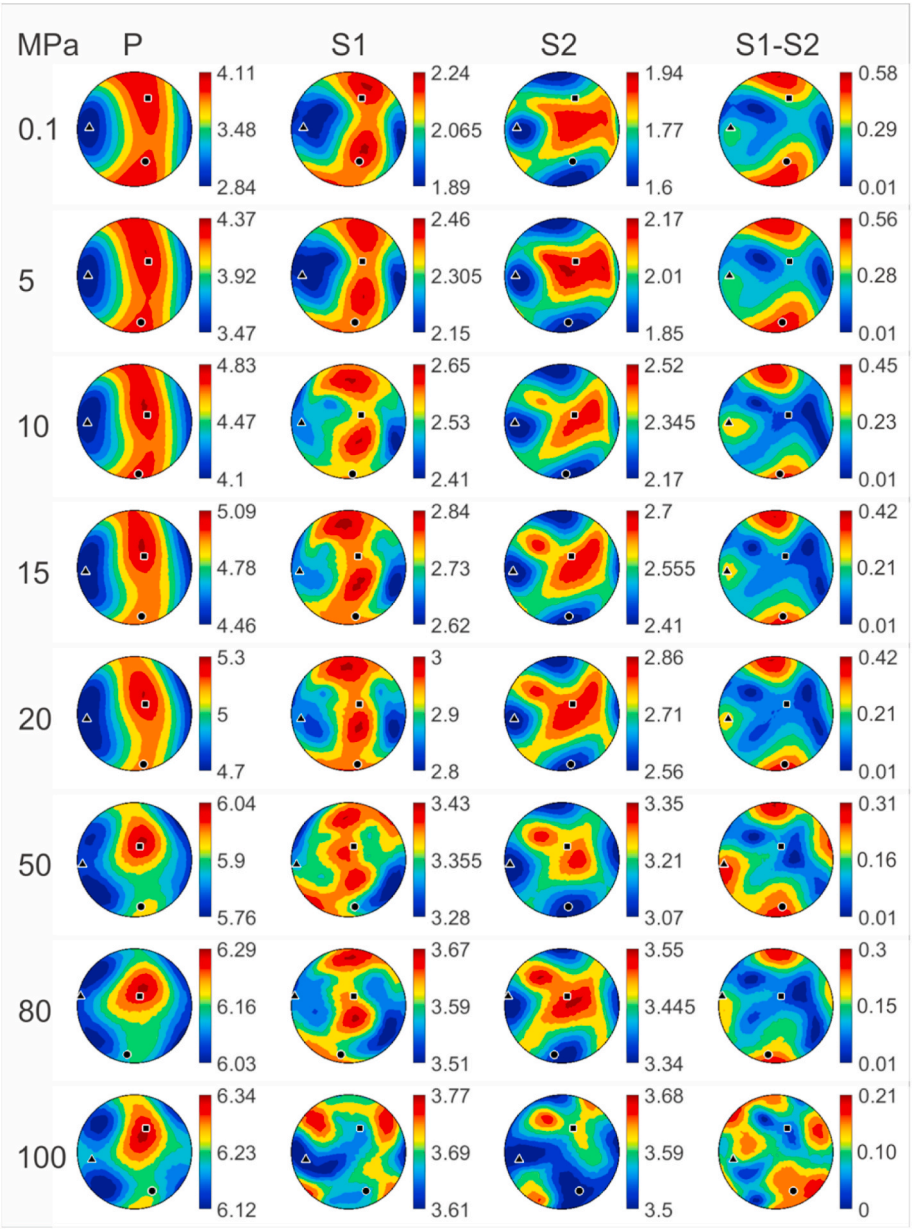

Fig. 3. The phase velocity distribution for the GRM sample plotted in the equal-area stereographic projection on the lower hemisphere. From left to right: velocities of the P, S1, S2 and the difference between the S1 and S2 velocities (in km/s). The pressure level increases from top to bottom. Stiffness tensor orientation is represented by the black symbols: square – x_1-axis (maximum P-wave velocity), circle – x_2-axis (intermediate P-wave velocity), triangle - x_3-axis (minimum P-wave velocity).

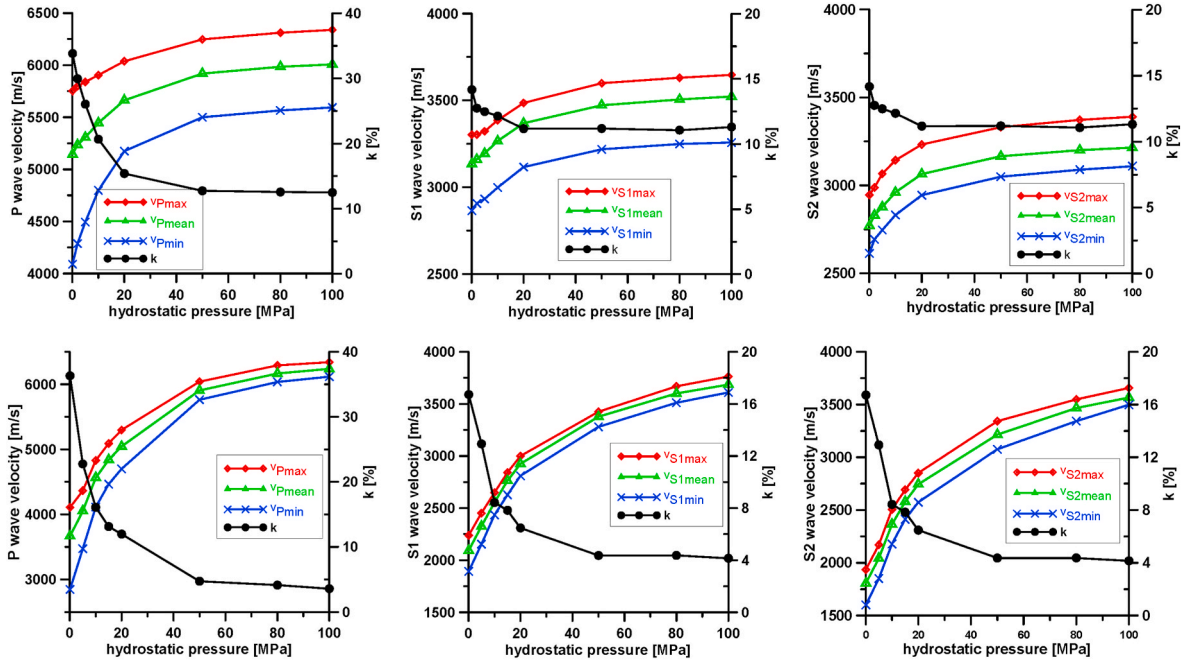

Fig. 4. The maximum, mean, and minimum phase velocity/pressure plots together with the coefficient of anisotropy $k = 100\ (v_{max}\text{-}v_{min})/v_{mean}$. From left to right: P, S1, S2 waves. Top: the BUK sample; bottom: the GRM sample.

tested rocks.

Fig. 4 displays the velocity/pressure dependency for three extreme directions together with the degree of anisotropy evaluated in percent, $k = 100(v_{max}\text{-}v_{min})/v_{mean}$). Based on these trends, we can distinguish between microcracks and rock-matrix dominated pressure ranges. In general, the crack closing pressure is estimated as a threshold between non-linear (crack closing) and linear (rock matrix dominated) velocity/pressure trends (e.g., Pros et al.[8]). For most rocks, it is expected to be within the range of 150–500 MPa.[54] However, for mantle rocks, Christensen[55] reported an influence of cracks up to 1000 MPa. In this work, the maximum applied pressure of 100 MPa was not high enough to close all the cracks and to reach the linear velocity/pressure trend. For these reasons, we used the anisotropy behavior to distinguish between the crack- and matrix-dominated pressure regions. However, this change in anisotropy behavior is related only to the influence of oriented cracks (e.g., Kern et al.[5]). For both samples, this threshold is between 20 and 50 MPa. Below this level, anisotropy steeply decreases with pressure; then it remains practically constant. The BUK sample displays a clear orthorhombic symmetry of rock matrix with the 12% anisotropy at 100 MPa when most of the cracks are already closed. At low pressures, the symmetry remains the same, but the level of anisotropy is increasing up to 32% for the P-wave velocity. This behavior is caused by cracks aligned with the foliation. The GRM sample is practically isotropic at 100 MPa ($k = 4\%$), while being transversely isotropic at low pressure ($k = 36\%$). This TI of the GRM sample is related to the preferential orientation of cracks and it is characteristic for granitic rocks.[17,18] Both rocks display a similar behavior of P- and S-wave anisotropy. Degree (strength) of the high-pressure anisotropy of the rock matrix is the same for both wave types. At low pressures, when the influence of oriented cracks is significant, degree of the P-wave anisotropy is about twice higher than that of the S-wave anisotropy.

5. Dynamic elastic parameters in the principal coordinate system

The procedure described in Section 2 was used to transform the stiffness tensors of the BUK and GRM samples from the coordinate systems chosen in the experiments to their principal coordinate systems. The types of the symmetry of anisotropy were determined using criteria summarized in Table 1. Then, the compliance tensors were calculated as the inverse of the stiffness tensors in the symmetry planes. The elastic constants were determined and their pressure dependencies were evaluated.

5.1. The stiffness tensor for the BUK and GRM samples

Tensors c_{ijkk} and c_{ilkl} have three distinct eigenvalues (132, 122, 76 GPa and 141, 127, 86 GPa) for the BUK sample under the atmospheric pressure. The three eigenvectors also satisfy Eq. (5) suggesting that the stiffness tensor c_{ijkl} is orthorhombic according to Table 1. The results obtained from Eqs (4) and (5) for the atmospheric pressure and 100 MPa are presented in Table 2. The results show small deviations from zero at

Table 2
Evaluation of the eigenvectors and eigenvalues of c_{ijkk} and c_{ilkl} for the BUK and GRM samples under pressures of 0.1 and 100 MPA based on Eq. (4) and Eq. (5).

Rock type	Matrix	Pressure (MPa)	Eigenvalues (GPa)			Residual of Eq. (5a) (GPa)			Residual of Eq. (5b) (GPa)			Mean of absolute residuals (GPa)
BUK	c_{ijkk}	0.1	132	122	76	−2.10	0.20	0.61	−1.47	−0.59	2.93	1.32
		100	177	168	155	1.52	−0.94	−1.03	1.38	−1.08	−3.27	1.54
	c_{ilkl}	0.1	141	127	86	0.51	−0.64	−0.61	1.47	−1.09	−0.17	0.75
		100	174	162	140	−0.82	−0.52	0.16	0.12	0.22	0.53	0.39
GRM	c_{ijkk}	0.1	81	75	47	−0.38	−1.22	−0.31	0.37	−0.33	−1.13	0.62
		100	186	180	179	−0.74	−1.66	0.51	−1.39	0.85	0.64	0.96
	c_{ilkl}	0.1	70	69	41	0.21	0.95	0.45	0.39	−0.08	0.38	0.41
		100	191	185	183	0.56	−0.79	0.00	1.51	0.21	0.82	0.65

Table 3
The elements of the stiffness tensor of the BUK sample in its principal coordinate system. Bolded are pressure levels closest to the in-situ conditions (~15 MPa).

Elements (GPa)	Pressure (MPa)							
	0.1	2	5	10	20	50	80	100
C_{11}	89.80	91.46	92.78	**94.97**	**99.38**	106.17	108.45	109.35
C_{22}	78.88	80.51	81.40	**83.89**	**89.13**	97.02	99.18	99.36
C_{33}	45.05	49.61	54.65	**62.60**	**72.92**	82.26	84.24	85.07
C_{44}	19.68	20.34	21.08	**22.39**	**24.02**	26.14	26.63	27.12
C_{55}	21.79	22.66	23.03	**24.18**	**26.07**	27.69	28.43	28.44
C_{66}	28.55	29.00	29.41	**30.78**	**32.52**	34.49	35.02	35.45
C_{12}	27.02	27.74	27.91	**27.30**	**28.57**	32.04	32.99	33.25
C_{13}	14.85	17.35	19.05	**22.93**	**27.53**	33.54	33.91	34.13
C_{23}	16.66	18.97	20.57	**24.35**	**29.92**	34.97	36.04	36.00
C_{14}	0.41	0.16	−0.11	**0.57**	**0.24**	0.35	0.10	−0.09
C_{15}	−0.51	−0.65	−0.66	**0.32**	**0.30**	0.18	−0.41	0.42
C_{16}	−1.06	−0.64	−0.69	**−0.59**	**−0.33**	−0.49	0.44	−0.43
C_{24}	0.05	0.05	0.09	**0.33**	**0.46**	0.31	0.36	0.47
C_{25}	3.78	3.09	2.87	**−2.34**	**−3.07**	−3.33	3.71	−3.76
C_{26}	−0.02	−0.16	−0.40	**−0.38**	**−0.36**	−0.24	0.31	−0.38
C_{34}	−0.91	−0.68	−0.70	**−0.41**	**−0.20**	−0.12	−0.06	−0.01
C_{35}	−0.55	−0.36	−0.19	**0.11**	**0.51**	0.36	−0.39	0.33
C_{36}	3.08	2.26	2.80	**2.53**	**2.02**	2.26	−2.03	2.36
C_{45}	−0.93	−0.66	−0.63	**−0.58**	**−0.64**	−0.80	0.52	−0.75
C_{46}	−1.66	−1.06	−1.16	**1.48**	**1.46**	2.25	−2.10	2.25
C_{56}	1.32	1.11	1.34	**−0.42**	**−0.76**	−0.74	−0.70	−0.84

the right-hand side of Eq. (5) since the material is not perfectly symmetric. The absolute sum of residuals does not exceed, however, an average of 1.54 GPa for the BUK sample, which is quite small compared to the elements of the stiffness tensor. By an ideal symmetric material, we mean a material with a stiffness tensor corresponding to one of the forms of symmetric tensors defined for the isotropic, transversely isotropic, and orthorhombic materials with exactly zero right-hand sides of Eq. (5). An example of an ideal orthorhombic tensor is presented in Appendix A.

One can use one of the two sets of the eigenvectors obtained from c_{ijkk} and c_{ilkl} to find the symmetry planes of the material. For example, the eigenvectors obtained from c_{ilkl} for the BUK sample under 0.1 and 100 MPa pressures (Table 2) have smaller average errors than those obtained from c_{ijkk}. In this case, it would be better to use the set of the eigenvectors that produces smaller errors according to Eq. (5). However, a more realistic way is using an average of the two sets of eigenvectors obtained from c_{ijkk} and c_{ilkl} to find the symmetry planes of the material.

Table 3 presents the elements of the stiffness tensors in the principal coordinate system for the BUK sample under various confining pressures obtained by the rotation of the initial tensors using Eq. (7). Constants C_{14} to C_{56} are expected to be zero in an ideal isotropic, transversely isotropic, and orthorhombic material. Moreover, $C_{11} = C_{22}$, $C_{44} = C_{55}$, and $C_{66} = (C_{11} - C_{12})/2$ for a transversely isotropic material. Since the rocks do not display a perfectly symmetric anisotropy, constants C_{14} to C_{56} are small but not exactly zero. Since these values are insignificant, we neglect them in physical interpretations.

For the GRM sample at atmospheric pressure, the c_{ilkl} has two equal eigenvalues 70 and 69 GPa (the third eigenvalue is 41 GPa) and three eigenvectors that satisfy Eq. (5) as presented in Table 2. Therefore, GRM can be considered as transversely isotropic at lower pressures (see Table 1). By applying higher confining pressures, the sample becomes closer to isotropy having three equal values satisfying Eq. (5). Note that the averages of the sum of absolute residuals of Eq. (5) $(0.62, 0.96, 0.41, 0.65$ GPa) are less for the GRM sample than those for the BUK sample $(1.32, 1.54, 0.75, 0.39$ GPa). This suggests that the symmetry planes in the GRM sample coincide better with the ideal cases. Again, by applying higher pressures, the GRM becomes closer to an isotropic rock.

The stiffness tensor of the GRM sample in its principal coordinate

Table 4
The elements of the stiffness tensor of the GRM sample in its principal coordinate system. Bolded are pressure levels closest to the in-situ conditions (~12 MPa).

Elements (GPa)	Pressure (MPa)							
	0.1	5	10	15	20	50	80	100
C_{11}	48.16	54.38	**66.76**	**74.09**	79.97	104.40	112.58	114.68
C_{22}	44.60	51.84	**64.94**	**71.30**	76.48	101.01	108.76	112.45
C_{33}	23.07	34.51	**48.43**	**57.00**	63.29	96.23	105.92	110.49
C_{44}	10.63	11.90	**14.43**	**17.41**	19.05	27.36	32.17	35.48
C_{55}	7.67	11.59	**16.86**	**19.93**	22.97	32.02	36.08	36.97
C_{66}	13.85	16.83	**18.96**	**22.11**	24.97	31.68	37.35	38.12
C_{12}	19.34	20.17	**25.81**	**26.57**	27.12	35.85	34.90	35.20
C_{13}	13.23	16.93	**20.41**	**22.36**	23.44	34.53	37.02	35.89
C_{23}	10.81	17.68	**23.70**	**25.37**	25.54	39.77	38.09	32.87
C_{14}	−1.18	0.27	**−0.57**	**0.26**	−0.96	−0.76	−0.07	−0.53
C_{15}	0.06	−0.23	**0.58**	**0.34**	0.16	−0.09	0.19	0.32
C_{16}	−0.30	0.24	**−0.05**	**0.41**	−0.73	−0.12	−1.12	0.76
C_{24}	0.53	−0.30	**−0.64**	**0.40**	0.11	0.30	−0.92	0.12
C_{25}	−1.70	1.98	**−0.03**	**−0.65**	−0.95	−1.09	−1.03	1.06
C_{26}	0.43	−0.21	**−0.47**	**0.43**	−0.06	−0.50	0.48	0.37
C_{34}	−0.29	0.35	**0.73**	**−0.16**	0.29	−0.45	0.65	0.42
C_{35}	0.36	−0.14	**−0.28**	**0.12**	0.28	0.52	0.38	−0.31
C_{36}	−0.98	−1.87	**−0.57**	**−0.03**	0.59	0.05	0.97	−3.03
C_{45}	0.73	1.80	**1.62**	**−1.65**	1.00	1.19	0.31	0.77
C_{46}	0.85	−1.25	**−0.56**	**−0.28**	0.07	0.24	−0.11	−1.08
C_{56}	0.70	−0.38	**0.40**	**−0.75**	0.16	1.07	0.60	−0.56

system is summarized in Table 4 for all confining pressures. The elements C_{14} to C_{56} are very small compared to the other elements and can be considered to be zero. At lower pressures, $C_{11} = C_{22}$, $C_{44} = C_{55}$, and $C_{66} = (C_{11} - C_{12})/2$, showing that the material is transversely isotropic and the plane of isotropy is 12. At higher pressures, this plane changes into 23 so $C_{22} = C_{33}$ and $C_{55} = C_{66}$.

5.2. The elastic parameters of the BUK and GRM samples

The compliance matrix **S** is obtained from the inverse of the stiffness matrix **C**, which has the following form for orthorhombic materials:

$$\mathbf{S} = \begin{bmatrix} \frac{1}{E_1} & -\frac{\nu_{21}}{E_2} & -\frac{\nu_{31}}{E_3} & 0 & 0 & 0 \\ & \frac{1}{E_2} & -\frac{\nu_{32}}{E_3} & 0 & 0 & 0 \\ & & \frac{1}{E_3} & 0 & 0 & 0 \\ & & & \frac{1}{G_{23}} & 0 & 0 \\ & & & & \frac{1}{G_{31}} & 0 \\ & & & & & \frac{1}{G_{12}} \end{bmatrix}. \quad (15)$$

The Young's and shear moduli as well as the Poisson's ratios within the three principal planes of the BUK and GRM samples are plotted in Fig. 5 and summarized in Table C1. For the BUK sample (Fig. 5a), the three Young's moduli at atmospheric pressure are $E_1 = 78$ GPa, $E_2 = 66$ GPa, and $E_3 = 40$ GPa. When increasing the pressure to 100 MPa, these values climb to $E_1 = 91$ GPa, $E_2 = 80$ GPa, and $E_3 = 67$ GPa, showing an increase of 17%, 21%, and 67% for directions 1, 2, 3, respectively. The highest rate of increase in Young's moduli is in the third direction that stems from a high density of oriented microcracks. Moreover, this increase mostly occurs at lower pressures up to 30 MPa; then the Young's moduli become stable. However, the BUK sample still behaves as an orthorhombic material even at the pressure of 100 MPa but with smaller anisotropy ratios of the Young's moduli. Remind that the Poisson's ratios ν_{31} and ν_{32} are the ratios of strains ε_1 and ε_2 to ε_3 when the loading is applied in direction 3, whereas ν_{21} is the ratio of ε_1 to ε_2 for the loading applied in direction 2. Both ν_{31} and ν_{32} of the BUK sample increase with pressure due to increasing stiffness in direction 3 caused by closing of microcracks parallel to the foliation (perpendicular to the direction 3). The decreasing trend of ν_{21} is rather surprising and points to a complex behavior of the crack-induced anisotropy during the crack closure. The observed decrease might be related to closing of preferentially oriented cracks, which can induce directionally dependent changes in grain boundary conditions in the foliation plane. The shear moduli increase with a similar rate under higher pressure for all three principal planes. This means that the shear moduli in the three principal planes are affected similarly by pressure. To summarize, the BUK sample behaves like an orthorhombic material even at higher

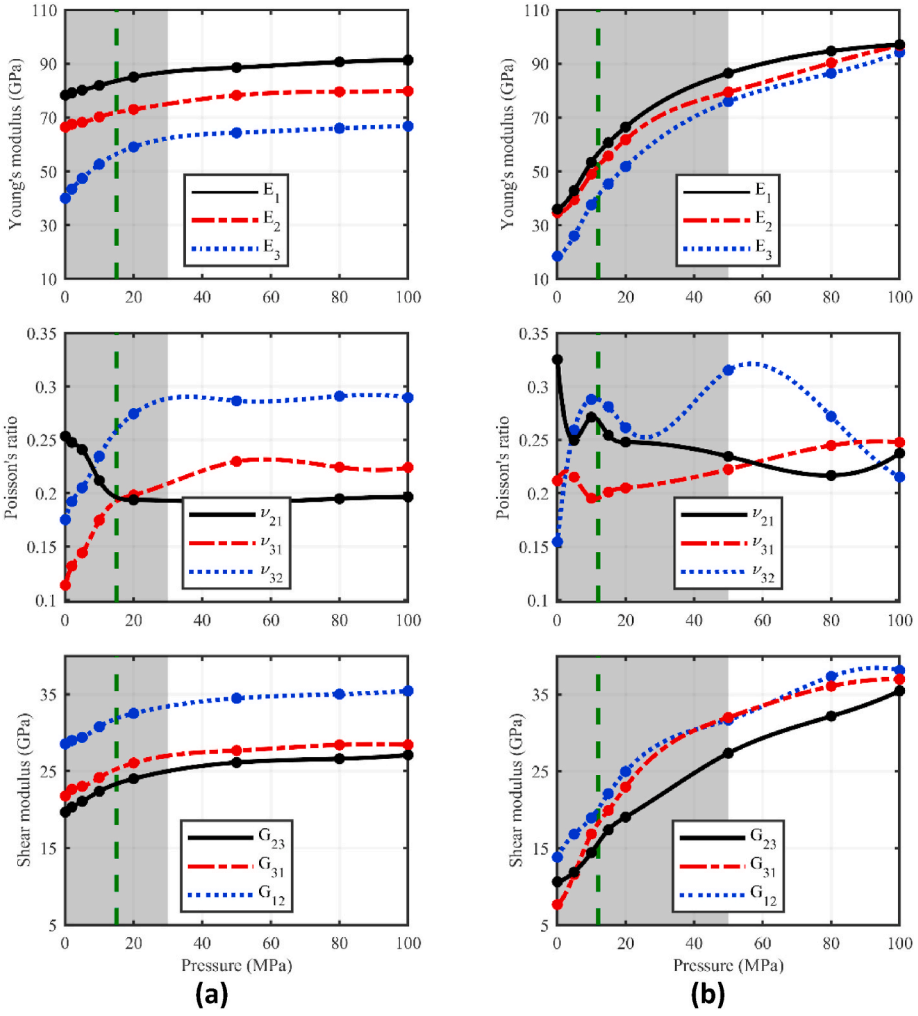

Fig. 5. Elastic parameters ($E_1, E_2, E_3, \nu_{21}, \nu_{31}, \nu_{23}, G_{23}, G_{31}, G_{12}$) in three principal planes for (a) the BUK sample and (b) the GRM sample. The values themselves can be found in Appendix C. The shaded region is dominated by the presence of cracks, the white region is controlled by the rock fabric. The border between both regimes represents a crack-closing pressure. The green dashed line corresponds to the expected lithostatic pressure at the URL. (For interpretation of the references to colour in this figure legend, the reader is referred to the Web version of this article.)

pressures although its behavior becomes closer to isotropic materials, especially above the pressure with limited influence of oriented cracks (30 MPa).

The variation of Young's moduli with pressure for the GRM sample in Fig. 5b shows that E_1 and E_2 are very close at atmospheric pressure, while E_3 is about half of the two others. With increasing pressure, all three Young's moduli converge. Besides, the Poisson's ratios and the shear moduli are smaller in planes 23, 13 than the ones in 12 at first, then become closer for the higher confining pressures. The GRM sample is transversely isotropic at atmospheric pressure, but the degree of anisotropy decreases in all three plots of Young's moduli, Poisson's ratios, and shear moduli. Hence, one may consider the GRM sample as transversely isotropic at atmospheric pressure but isotropic at 100 MPa.

What is striking about the comparison of the elastic parameters of the two rocks is that the Young's and shear moduli at atmospheric pressure for GRM ($E_1 = 36$ GPa, $E_2 = 35$ GPa, and $E_3 = 18$ GPa) are smaller than the ones for the BUK ($E_1 = 78$ GPa, $E_2 = 66$ GPa, and $E_3 = 40$ GPa) suggesting that the BUK is denser than the GRM. At 100 MPa pressure, these values increase dramatically in the GRM ($E_1 = 97$ Gpa, $E_2 = 97$ GPa, and $E_3 = 94$ GPa) and become higher than the corresponding values for the BUK ($E_1 = 91$ GPa, $E_2 = 80$ GPa, and $E_3 = 67$ GPa). By increasing the pressure, all these moduli increase in the GRM sample due to the crack closure which makes the material more intact. However, a great portion of anisotropy in the BUK sample originates from texture anisotropy and will not be reduced due to pressure.

6. Discussion

In this section, the reasons behind the different behavior of the GRM and BUK samples under various confining pressures are discussed in detail. Moreover, the orientation stability of the principal coordinate systems with pressure is evaluated. Finally, the obtained results are compared to those already published and the expected properties at the in situ URL depths are summarized.

6.1. Change in anisotropy ratios of the elastic constants with pressure

Fig. 6 shows normalized values of elastic constants for the BUK and GRM samples as a function of pressure. These values represent anisotropy ratios of the elastic constants in the three principal axes. The ratios E_2/E_3 and E_1/E_3 describe the behavior in two symmetry planes perpendicular to the foliation symmetry plane, which itself is characterized by the E_1/E_2. The closer all these values get to the unity, the more isotropic the material is. As mentioned above, the pressure dependencies can be divided into two characteristic regions: (1) low pressure, dominated by the crack influence, (2) high pressure, dominated by properties of the rock matrix. Due to the low maximum pressure used in the experiment (100 MPa), some of the cracks remained open even at the highest pressures linear velocity/pressure trends were not reached. To distinguish between crack- and matrix-dominated pressure ranges, we used the change in anisotropic behavior that should be related only to the oriented cracks. We defined the "crack-closing pressure" for oriented cracks as a pressure, for which the E_1/E_3 ratio decreased by 90% from its

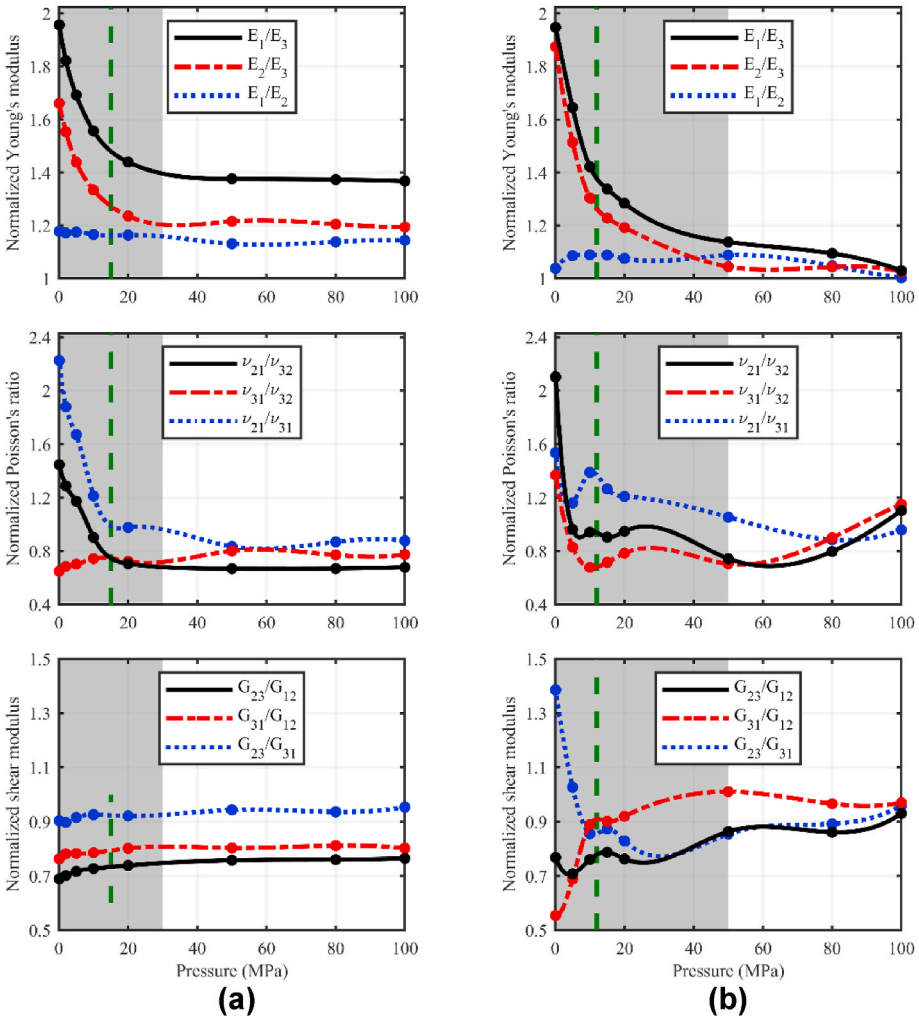

Fig. 6. Normalized elastic parameters in three principal planes for (a) the BUK sample and (b) the GRM sample. The shaded region is dominated by the presence of cracks, the white region is controlled by the rock fabric. The border between both regimes represents a crack-closing pressure. The green dashed line corresponds to the expected lithostatic pressure at the URL. (For interpretation of the references to colour in this figure legend, the reader is referred to the Web version of this article.)

initial value. It was found to be 30 MPa for BUK and 50 MPa for the GRM sample, respectively. Above this level, the influence of oriented cracks was insignificant.

As documented by the trends of E_2/E_3 and E_1/E_3 , both rocks display high anisotropy at low pressure related to the crack system parallel to the foliation. On the other hand, the E_1/E_2 ratios are independent of the pressure. This might be explained as follows: (1) no cracks are perpendicular to the foliation; (2) two equal crack systems are perpendicular to the symmetry axes directions 1 and 2; and (3) cracks perpendicular to the foliation have a random azimuthal distribution. The type (1) interpretation may correspond to the BUK sample, where the influence of the cracks perpendicular to the foliation is marginal (see Fig. 6a). The type (3) interpretation can explain the behavior of heavily cracked GRM sample. The E_1/E_2 ratio is ~1.2 for the BUK sample but ~1.03 for the GRM sample. This illustrates a difference between orthorhombic anisotropy (BUK) and transverse isotropy (GRM) with a symmetry plane in the foliation. Above the crack-closing pressure, the ratio trends stabilize and reflect the anisotropy of the rock matrix. At 100 MPa, the BUK sample displays ratios within 1.1-1.3 range. On the other hand, the GRM sample becomes practically isotropic with ratios below 1.1.

The interpretation of trends for the normalized Poisson's ratio and normalized shear moduli with pressure is more difficult, because it relates the behavior of two symmetry planes. Nevertheless, the trends are in general similar to those of the Young moduli. The ratios are getting closer to one with increasing pressure as the cracks are closing. The pressure changes are more distinct for the GRM sample, which has high microcrack content. After the crack closure, the BUK sample remains anisotropic and the GRM displays practically isotropic behavior.

6.2. Orientation of the principal stiffness tensor

Figs. 2 and 3 show anisotropic distributions of velocities together with axes of the principal coordinate system. In general, axes x_1 and x_2 (corresponding to the C_{11} and C_{22} stiffness constants) lie within the high P-wave velocity plane of foliation. The x_1-axis fits well to the highest velocity directions identifying the lineation. The x_3-axis (corresponding to the C_{33} stiffness constant) lies within the minimum velocity area that is perpendicular to the foliation and to the dominant microcrack system as well. A similar relation can be observed for the S1 wave anisotropy but the maximum velocity regions are about 45° rotated when compared to the direction of the maximum stiffness. On the other hand, the regions of the maximum S2 velocity are completely out of the foliation plane. The complexities in the S-wave velocity distributions are often predicted for theoretical anisotropy models as well as measured for real rocks.[56–58]

Fig. 7 displays the pressure-induced changes in the orientation of the principal coordinate system. For the BUK sample, the orientation of anisotropy axes is stable and independent of the applied pressure. Consequently, the microcrack anisotropy and the fabric-induced anisotropy have likely parallel orientations, otherwise, a rotation of symmetry axes should be observed.[59] The GRM sample displays a scattering in the pressure-dependent orientation of anisotropy axes, especially, at low and high pressures (Fig. 7b). At the low pressure, it may be a combined effect of uneven microcrack closing and isotropy in the foliation plane. At the high pressure, it may be an effect of heterogeneity of the GRM sample.

6.3. Comparison of the elastic constants with other reported results

The elastic constants of the GRM sample measured under the atmospheric pressure are compared with those from other studies (Table 5). In this paper, no presumption about anisotropy symmetry is considered and the elastic constants of the GRM are obtained in the most general form. By contrast, previous works assumed the GRM sample as a transversely isotropic material and considered some other presumptions to obtain the elastic constants.

Since a transversely isotropic rock has five independent elastic constants $(E_1 = E_2, E_3, G_{23} = G_{31}, \nu_{21}, \nu_{31} = \nu_{32})$ while only four independent strain measurements of a single uniaxial compression test are available, one elastic constant remains undetermined. Hence, Nejati[60] assumed the Saint-Venant relation as the fifth constraint and obtained the static constants of GRM samples from the uniaxial compression test (average of S1, S2, and S3 in Table 3 from Nejati[60]). Nejati et al.[47] obtained the four elements of the dynamic stiffness matrix (C_{11}, C_{13}, C_{33}, and C_{44}) by fitting the velocity obtained from P-wave measurements against the polar angle. As the fifth constraint, Nejati et al.[47] assumed three alternative values for the in-plane Poisson's ratio (ν_{21}). They considered $\nu_{21} = 0.1, 0.2, 0.3$ and presented the resulting tangent elastic constants for this whole range under a zero confinement. Here, we chose the results reported for $\nu_{21} = 0.3$, which we consider as most realistic. In Table 5, we have provided an average of three tested samples (the average of S1, S2, and S3 when $\nu_d = 0.3$ is assumed in Table 6 from Nejati et al.[47]). The dynamic constants are often expected to be higher than the static ones,[61] although exceptions are reported in the literature.[48]

In addition, elastic constants determined for the BUK sample in this study are compared with those obtained from a cyclic uniaxial loading of cylindrical samples. The migmatized gneiss was considered to be transversely isotropic, and several cylindrical samples with the symmetry plane (foliation) normal, parallel, and inclined (45°) to the loading axis were tested. Here we present the elastic constants estimated from the first cycle with the uniaxial loading range of 7–21 MPa (Table 6). As expected, the obtained static moduli are smaller than their

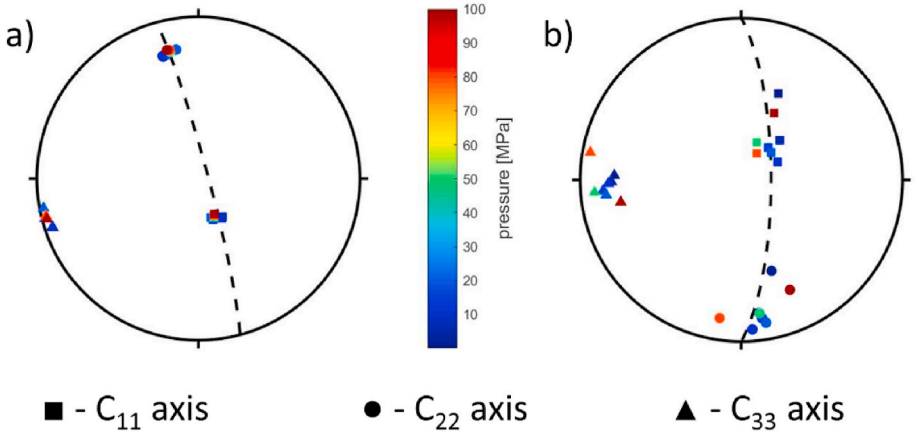

Fig. 7. Pressure dependent orientation of stiffness tensor plotted in the equal-area stereographic projection on the lower hemisphere. The dashed line represents the foliation plane. (a) the BUK sample; (b) the GRM sample.

Table 5
Elastic constants of the GRM sample based on different testing methods. The previous studies assumed the GRM to be transversely isotropic and used the Saint-Venant assumption and $\nu_{21} = 0.3$ to find the static and dynamic elastic constants, respectively.

Parameter type	Test	E_1 (GPa)	E_2 (GPa)	E_3 (GPa)	G_{23} (GPa)	G_{31} (GPa)	G_{12} (GPa)	ν_{21}	ν_{31}	ν_{32}	Reference
Static	Uniaxial compression	29.1	29.1	7.6	8.2	8.2	12.1	0.17	−0.04	−0.04	Nejati[60]
Dynamic	Ultrasound (Cylinder)	38.7	38.7	19.9	11.1	11.1	14.9	0.30	0.04	0.04	Nejati et al.[47]
	Ultrasound (Sphere)	36	35	18	11	8	14	0.33	0.21	0.15	This study

Table 6
Elastic constants of the BUK sample based on two testing methods. The BUK is presumed to be transversely isotropic.

Sample shape	Test		E_1 (GPa)	E_2 (GPa)	E_3 (GPa)	ν_{21}	ν_{31}	ν_{32}
Cylinder	Cyclic	Loading	66	24	24	0.33	0.06	0.06
		Unloading	73	32	32	0.27	0.09	0.09
Sphere	Ultrasound		78	66	40	0.25	0.11	0.18

dynamic equivalents from the present study. However, the values become closer, if we consider the unloading part of the test, which is less influenced by pre-existing cracks. Note that these values become even closer if we consider the following cycles for which the upper loading limit gradually increases up to 72 MPa.

6.4. The expected properties at the in situ URL depths

Both tested samples come from the URLs related to research of a long-term deposition of a nuclear waste. The expected depth of such a repository is about 300–500 m. In this study, we consider the in situ depths of URLs and the corresponding lithostatic pressure caused by overburden rocks. These are 550 m and 15 MPa for the Bukov URL and 400 m and 12 MPa for the Grimsel URL, as is highlighted in Figs. 5 and 6 and Tables 3 and 4 At 15 MPa, the BUK sample displays orthorhombic symmetry described by the engineering constants: $E_1 = 84$ GPa, $E_2 = 71$ GPa, and $E_3 = 56$ GPa; $G_{12} = 32$ GPa, $G_{13} = 25$ GPa, and $G_{23} = 23$ GPa; $\nu_{21} = 0.19$, $\nu_{31} = 0.19$, and $\nu_{32} = 0.27$. These values were obtained from a spline approximation between the nearest measured pressure levels (see Table C1 in Appendix C). The in-situ pressure is within the crack dominated range (below 30 MPa) and based on the normalized Young moduli (Fig. 6a), we can expect some of the cracks with preferential orientation being still open.

At the 12 MPa, the GRM sample displays transverse isotropy that is described by the engineering constants: $E_1 = 56$ GPa, $E_2 = 52$ GPa, and $E_3 = 41$ GPa; $G_{12} = 20$ GPa, $G_{13} = 19$ GPa, and $G_{23} = 15$ GPa; $\nu_{21} = 0.27$, $\nu_{31} = 0.20$, and $\nu_{32} = 0.28$. They were estimated in the same way as for the BUK sample, moreover, the appropriate pairs (E_1, E_2; ν_{13}, ν_{23}; G_{13}, G_{12}) can be averaged to get the TI constants. The in-situ pressure is well within the crack dominated range (50 MPa) and based on the normalized Young moduli (Fig. 6a) and exponential velocity/pressure trend in Fig. 4, we can expect a significant influence of cracks. The orientation of the principal coordinate system coincides with the orientation of the texture for both tested samples. The x_3-axis (corresponding to the C_{33} stiffness constant) is perpendicular to the foliation and the x_1-axis (corresponding to the C_{11} stiffness constant) is parallel to the lineation.

7. Conclusions

We arrived at the following conclusions:

- Analyzing the stiffness tensor of an anisotropic rock, which is defined by 21 elastic constants measured in an arbitrarily oriented coordinate system, we can identify the symmetry type of anisotropy and transform the stiffness tensor into its principal coordinate system. To achieve this, we have developed a method (based on a previously proposed method for ideal stiffness tensors) in a way to be used for experimental noisy data.
- The Bukov migmatized gneiss displays orthorhombic symmetry at all pressures, whereas the Grimsel granite is transversely isotropic under the atmospheric pressure and becomes almost isotropic at high pressures.
- The orientation of anisotropy axes agrees well with the orientation of structural elements for both rocks. The minimum P-wave velocity is perpendicular to the foliation, while the maximum P-wave velocity is parallel to the lineation in the foliation plane. The preferential crack systems are parallel to the foliation for both the BUK and GRM samples. Additionally, the GRM sample probably contains cracks perpendicular to the foliation with a random azimuthal orientation.
- At lower pressures, the anisotropy of both samples is highly influenced by the presence of oriented cracks. Their influence is marginal above the 30 and 50 MPa for the BUK and GRM samples, respectively. The degree of anisotropy decreases with increasing pressure, while its orientation remains unchanged. The decrease of anisotropy degree is likely caused by closing the crack systems parallel to the foliation. Once the cracks are closed, the BUK sample remains orthorhombic, while the GRM sample becomes isotropic.
- Both rocks are anisotropic under the equivalent of the overburden pressure acting at the in-situ URL conditions. The Bukov migmatized gneiss is orthorhombic, while the Grimsel Aare granite is transversely isotropic. A significant amount of cracks remains open at these pressures and contribute to the overall anisotropy of rocks.
- The presented results agree well with those reported previously in the literature being obtained under a priori presumption about the type and orientation of the anisotropy symmetry. The presented approach is more general and thus preferable, in particular, if the anisotropy symmetry of a rock is not obvious.

Declaration of competing interest

The authors declare that they have no known competing financial interests or personal relationships that could have appeared to influence the work reported in this paper.

Acknowledgment

We thank Douglas Schmitt and two anonymous reviewers for their

detailed and helpful comments. The study was partially supported by the Czech Science Foundation research grants CSF 21-26542S and 22-00580S, by the Czech Academy of Sciences projects RVO 67985831 and RVO 68145535, and by the project of JINR theme No.: 04-4-1142-2021/2025. We gratefully acknowledge the partial support of the Project of the Institute of Clean Technologies for Mining and Utilization of Raw Materials for Energy Use under National Sustainability Program I (LO1406). This work was kindly supported by the SURAO projects "Research Support for Safety Evaluation of Deep Geological Repository" and "Data acquisition from deep horizons of Rožná mine".

Open-public MATLAB code SYMMETRY.m (https://www.ig.cas.cz/symmetry-code/) for identification of the type of anisotropy symmetry and the orientation of the principal coordinate system from a general stiffness tensor is provided in the Supplement.

Supplementary data

Supplementary data to this article can be found online at https://doi.org/10.1016/j.ijrmms.2022.105168.

Appendix A. Example of transforming an orthorhombic anisotropy into the principal coordinate system

Consider stiffness matrix $\mathbf{C}^*$ describing an orthorhombic symmetry with nine independent parameters for a single crystal of calcium sulfate in its principal coordinate system reported by Simmons and Wang[62]:

$$\mathbf{C}^* = \begin{bmatrix} 185 & 32 & 16 & 0 & 0 & 0 \\ & 112 & 15 & 0 & 0 & 0 \\ & & 94 & 0 & 0 & 0 \\ & & & 26 & 0 & 0 \\ & & & & 9 & 0 \\ & & & & & 32 \end{bmatrix}. \tag{A1}$$

The matrix contains 12 zero elements in the upper half of the matrix. Now, let us rotate the coordinate system by a clockwise rotation of 45° about the third axis. Based on Eq. (13), we transform the matrix $\mathbf{C}^*$ using the coordinate transformation matrix $\mathbf{\Omega}$ to obtain matrix $\mathbf{C}$ in a new coordinate system that does not coincide with the symmetry planes:

$$\mathbf{\Omega} = \begin{bmatrix} \cos(\pi/4) & \sin(\pi/4) & 0 \\ -\sin(\pi/4) & \cos(\pi/4) & 0 \\ 0 & 0 & 1 \end{bmatrix}, \tag{A2a}$$

$$\mathbf{K} = \begin{bmatrix} 0.5 & 0.5 & 0 & 0 & 0 & 1 \\ 0.5 & 0.5 & 0 & 0 & 0 & -1 \\ 0 & 0 & 1 & 0 & 0 & 0 \\ 0 & 0 & 0 & 0.7 & -0.7 & 0 \\ 0 & 0 & 0 & 0.7 & 0.7 & 0 \\ -0.5 & 0.5 & 0 & 0 & 0 & 0 \end{bmatrix}, \tag{A2b}$$

$$\mathbf{C} = \mathbf{K}\mathbf{C}^*(\mathbf{K})^T = \begin{bmatrix} 123 & 58 & 16 & 0 & 0 & -18 \\ & 123 & 16 & 0 & 0 & -18 \\ & & 94 & 0 & 0 & -1 \\ & & & 18 & 8 & 0 \\ & & & & 18 & 0 \\ & & & & & 58 \end{bmatrix}. \tag{A2c}$$

Since the matrix is not in the principal coordinate system, some zero-elements in Eq. (A1) disappeared. Hence, matrix $\mathbf{C}$ can simulate a general stiffness tensor in an arbitrary coordinate system obtained by the inversion of ultrasonic measurements. Now, we use the procedure proposed in section 2 to determine the symmetry type of matrix $\mathbf{C}$ and rotate it into its principal coordinate system. Matrices $\mathbf{U}$ and $\mathbf{V}$ (the expanded forms of the tensors c_{ijkk} and c_{isks}) are calculated using Eq. (4) and their eigenvectors ($\mathbf{\Omega}$) and eigenvalues ($\mathbf{E}$) are determined:

$$\mathbf{U} = \begin{bmatrix} 196 & -37 & 0 \\ & 196 & 0 \\ & & 125 \end{bmatrix}, \quad \mathbf{E}_1 = \begin{bmatrix} 234 \\ 159 \\ 125 \end{bmatrix}, \quad \mathbf{\Omega}_1 = \begin{bmatrix} -0.7 & 0.7 & 0 \\ & 0.7 & 0 \\ & & 1 \end{bmatrix}. \tag{A3}$$

$$\mathbf{V} = \begin{bmatrix} 199 & -28 & 0 \\ & 199 & 0 \\ & & 130 \end{bmatrix}, \quad \mathbf{E}_2 = \begin{bmatrix} 227 \\ 171 \\ 130 \end{bmatrix}, \quad \mathbf{\Omega}_2 = \begin{bmatrix} 0.7 & -0.7 & 0 \\ & 0.7 & 0 \\ & & 1 \end{bmatrix}. \tag{A4}$$

All three eigenvalues given in vectors $\mathbf{E}_1, \mathbf{E}_2$ are distinct and their eigenvectors in $\mathbf{\Omega}_1$, $\mathbf{\Omega}_2$ satisfy Eq. (4). Thus, matrix $\mathbf{C}$ is orthorhombic according to Table 1. Now, Eq. (13) is used to write the matrix $\mathbf{C}$ back in the principal coordinate system:

$$\mathbf{\Omega}_1 = \begin{bmatrix} -0.7 & 0.7 & 0 \\ & 0.7 & 0 \\ & & 1 \end{bmatrix}, \mathbf{\Omega}_2 = \begin{bmatrix} 0.7 & -0.7 & 0 \\ & 0.7 & 0 \\ & & 1 \end{bmatrix} \tag{A5a}$$

$$\mathbf{K}_1 = \begin{bmatrix} 0.5 & 0.5 & 0 & 0 & 0 & -1 \\ 0.5 & 0.5 & 0 & 0 & 0 & 1 \\ 0 & 0 & 1 & 0 & 0 & 0 \\ 0 & 0 & 0 & 0.7 & 0.7 & 0 \\ 0 & 0 & 0 & -0.7 & 0.7 & 0 \\ 0.5 & -0.5 & 0 & 0 & 0 & 0 \end{bmatrix}, \quad \mathbf{K}_2 = \begin{bmatrix} 0.5 & 0.5 & 0 & 0 & 0 & -1 \\ 0.5 & 0.5 & 0 & 0 & 0 & 1 \\ 0 & 0 & 1 & 0 & 0 & 0 \\ 0 & 0 & 0 & 0.7 & 0.7 & 0 \\ 0 & 0 & 0 & 0.7 & -0.7 & 0 \\ -0.5 & 0.5 & 0 & 0 & 0 & 0 \end{bmatrix}, \tag{A5b}$$

$\mathbf{C}^* = \mathbf{K}_i\mathbf{C}(\mathbf{K}_i)^T$ where for both, $i = 1, 2,$ we get the following identical result:

$$\mathbf{C}^* = \begin{bmatrix} 185 & 32 & 16 & 0 & 0 & 0 \\ & 112 & 15 & 0 & 0 & 0 \\ & & 94 & 0 & 0 & 0 \\ & & & 26 & 0 & 0 \\ & & & & 9 & 0 \\ & & & & & 32 \end{bmatrix}. \tag{A5c}$$

Appendix B. Relation between Euler angles and matrix Ω

The three Euler angles are widely used for representing the transformation of an orthogonal coordinate system in a three-dimensional space, although there are various definitions how to employ them. Here, we chose the definition presented by Rose,[63] in which the rotation is defined as the product of three Euler rotations to rotate the coordinate system from 123 to $1'''2'''3'''$ as illustrated in Fig. B1. In the three rotation steps, α is the rotation angle around axis 3, β is the rotation angle around axis $2''$, and Υ is the rotation angle around the axis $3'''$.

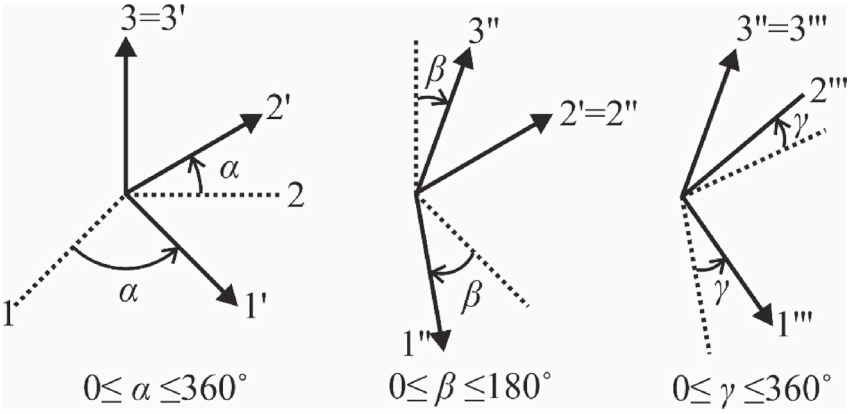

Fig. B.1. Three-step rotation of a coordinate system based on the Euler angles.

The rotations matrix is defined as:

$$\mathbf{\Omega} = \begin{bmatrix} \cos(\alpha)\cos(\beta)\cos(\gamma) - \sin(\alpha)\sin(\gamma) & \sin(\alpha)\cos(\beta)\cos(\gamma) + \cos(\alpha)\sin(\gamma) & -\sin(\beta)\cos(\gamma) \\ -\cos(\alpha)\cos(\beta)\sin(\gamma) - \sin(\alpha)\cos(\gamma) & -\sin(\alpha)\cos(\beta)\sin(\gamma) + \cos(\alpha)\cos(\gamma) & \sin(\beta)\sin(\gamma) \\ \cos(\alpha)\sin(\beta) & \sin(\alpha)\sin(\beta) & \cos(\beta) \end{bmatrix}. \tag{B1}$$

In our study, matrix $\mathbf{\Omega}$ was directly calculated, hence we did not have to calculate the Euler angles. However, one can readily find the Euler angles from Eq. (B1) whenever it is needed.

Appendix C. Elastic constants

Elastic constants of the BUK and GRM samples are summarized in Table C1.

Table C.1
Elastic constants of the GRM and BUK samples based on different testing methods. Bolded are pressure levels closest to the in-situ conditions

Sample	Confining pressure (MPa)	E_1 (GPa)	E_2 (GPa)	E_3 (GPa)	G_{23} (GPa)	G_{31} (GPa)	G_{12} (GPa)	$\nu 21$	$\nu 31$	$\nu 32$
BUK	0.1	78	66	40	20	22	29	0.25	0.11	0.18
	2	79	68	43	20	23	29	0.25	0.13	0.19
	5	80	68	47	21	23	29	0.24	0.14	0.21
	10	**82**	**70**	**53**	**22**	**24**	**31**	**0.21**	**0.17**	**0.23**
	20	**85**	**73**	**59**	**24**	**26**	**33**	**0.19**	**0.20**	**0.27**
	50	89	78	64	26	28	34	0.19	0.23	0.29
	80	91	80	66	27	28	35	0.19	0.22	0.29
	100	91	80	67	27	28	35	0.20	0.22	0.29
GRM	0.1	36	35	18	11	8	14	0.33	0.21	0.15
	5	43	39	26	12	12	17	0.25	0.22	0.26
	10	**53**	**49**	**38**	**14**	**17**	**19**	**0.27**	**0.20**	**0.29**
	15	**61**	**56**	**45**	**17**	**20**	**22**	**0.25**	**0.20**	**0.28**
	20	66	62	52	19	23	25	0.25	0.20	0.26
	50	86	79	76	27	32	32	0.23	0.22	0.32
	80	95	90	86	32	36	37	0.22	0.24	0.27
	100	97	97	94	35	37	38	0.24	0.25	0.22

References

1 Karato S-I. Seismic anisotropy due to lattice preferred orientation of minerals: kinematic or dynamic?. In: *High-Pressure Research in Mineral Physics: A Volume in Honor of Syun-iti Akimoto*. American Geophysical Union (AGU); 1987:455–471. https://doi.org/10.1029/GM039p0455.

2 Wenk H-R, Vasin R, Kern H, Matthies S, Vogel S, Ivankina T. Revisiting elastic anisotropy of biotite gneiss from the Outokumpu scientific drill hole based on new texture measurements and texture-based velocity calculations. *Tectonophysics*. 2012; 570–571:123–134. https://doi.org/10.1016/j.tecto.2012.06.023.

3 Ji S, Shao T, Michibayashi K, et al. Magnitude and symmetry of seismic anisotropy in mica- and amphibole-bearing metamorphic rocks and implications for tectonic interpretation of seismic data from the southeast Tibetan Plateau. *J Geophys Res Solid Earth*. 2015;120(9):6404–6430. https://doi.org/10.1002/2015JB012209.

4 Mainprice D. Seismic anisotropy of the deep earth from a mineral and rock physics perspective. In: Schubert G, Price G, eds. *Treatise on Geophysics*. third ed. vol. 2. Wiley; 2007:437–492. https://doi.org/10.1016/B978-044452748-6/00045-6.

5 Kern H, Ivankina TI, Nikitin AN, Lokajicek T, Pros Z. The effect of oriented microcracks and crystallographic and shape preferred orientation on bulk elastic anisotropy of a foliated biotite gneiss from Outokumpu. *Tectonophysics*. 2008;457(3): 143–149. https://doi.org/10.1016/j.tecto.2008.06.015.

6 Almqvist BSG, Mainprice D. Seismic properties and anisotropy of the continental crust: predictions based on mineral texture and rock microstructure. *Rev Geophys*. 2017;55(2):367–433. https://doi.org/10.1002/2016RG000552.

7 Rasolofosaon P. Stress-induced seismic anisotropy revisited. *Rev Inst Fr Pét.* 1998;53 (5):679–692. https://doi.org/10.2516/ogst:1998061.

8 Pros Z, Lokajíček T, Klíma K. Laboratory approach to the study of elastic anisotropy on rock samples. In: *Pure and Applied Geophysics*. vol. 151. 1998:619–629. https://doi.org/10.1007/s000240050133.

9 Wang W, Schmitt DR, Li W. A program to forward model the failure pattern around the wellbore in elastic and strength anisotropic rock formations. *Int J Rock Mech Min Sci*. 2022;151, 105035. https://doi.org/10.1016/J.IJRMMS.2022.105035.

10 Setiawan NB, Zimmerman RW. Wellbore breakout prediction in transversely isotropic rocks using true-triaxial failure criteria. *Int J Rock Mech Min Sci*. 2018;112: 313–322.

11 Krietsch H, Gischig V, Evans K, et al. Stress measurements for an in situ stimulation experiment in crystalline rock: integration of induced seismicity, stress relief and hydraulic methods. *Rock Mech Rock Eng.* 2019;52(2):517–542.

12 Ma T, Liu Y, Chen P, Wu B, Fu J, Guo Z. Fracture-initiation pressure prediction for transversely isotropic formations. *J Pet Sci Eng*. 2019;176:821–835. https://doi.org/10.1016/j.petrol.2019.01.090.

13 Moukhtari FE, Lecampion B, Zia H. Planar hydraulic fracture growth perpendicular to the isotropy plane in a transversely isotropic material. *J Mech Phys Solid*. 2020; 137. https://doi.org/10.1016/j.jmps.2020.103878.

14 Motra HB, Mager J, Ismail A, et al. Determining the influence of pressure and temperature on the elastic constants of anisotropic rock samples using ultrasonic wave techniques. *J Appl Geophys*. 2018;159:715–730. https://doi.org/10.1016/j.jappgeo.2018.10.016.

15 Bakulin A, Grechka V, Tsvankin I. Estimation of fracture parameters from reflection seismic data—Part II: fractured models with orthorhombic symmetry. *Geophysics*. 2000;65(6):1803–1817. https://doi.org/10.1190/1.1444864.

16 Takemura T, Golshani A, Oda M, Suzuki K. Preferred orientations of open microcracks in granite and their relation with anisotropic elasticity. *Int J Rock Mech Min Sci*. 2003;40(4):443–454. https://doi.org/10.1016/S1365-1609(03)00014-5.

17 Sano O, Kudo Y, Mizuta Y. Experimental determination of elastic constants of Oshima granite, Barre granite, and Chelmsford granite. *J Geophys Res Solid Earth*. 1992;97(B3):3367–3379. https://doi.org/10.1029/91JB02934.

18 Panaghi K, Golshani A, Sato M, Takemura T, Takahashi M. Crack tensor-based evaluation of inada granite behavior due to damage under true-triaxial testing condition. *Int J Rock Mech Min Sci*. 2018;106:30–40. https://doi.org/10.1016/j.ijrmms.2018.04.005.

19 Bakulin A, Grechka V, Tsvankin I. Estimation of fracture parameters from reflection seismic data—Part III: fractured models with monoclinic symmetry. *Geophysics*. 2000;65(6):1818–1830. https://doi.org/10.1190/1.1444865.

20 Aydin A. Upgraded ISRM suggested method for determining sound velocity by ultrasonic pulse transmission technique. *Rock Mech Rock Eng*. 2014;47(1):255–259. https://doi.org/10.1007/s00603-013-0454-z.

21 Liao JJ, Ting-Bin HU, Chang CW. Determination of dynamic elastic constants of transversely isotropic rocks using a single cylindrical specimen. *Int J Rock Mech Min Sci*. 1997;34(7):1045–1054.

22 Sarout J, Molez L, Guéguen Y, Hoteit N. Shale dynamic properties and anisotropy under triaxial loading: experimental and theoretical investigations. *Phys Chem Earth*. 2007;32(8-14):896–906. https://doi.org/10.1016/j.pce.2006.01.007.

23 Li W, Schmitt DR, Chen X. Accounting for pressure-dependent ultrasonic beam skew in transversely isotropic rocks: combining modelling and measurement of anisotropic wave speeds. *Geophys J Int*. 2020;221(1):231–250. https://doi.org/10.1093/gji/ggz580.

24 Van Buskirk WC, Cowin SC, Ward RN. Ultrasonic measurement of orthotropic elastic constants of bovine femoral bone. *J Biomech Eng*. 1981;103(2):67–72. https://doi.org/10.1115/1.3138262.

25 Svitek T, Vavryčuk V, Lokajíček T, Petružálek M. Determination of elastic anisotropy of rocks from P- and S-wave velocities: numerical modelling and lab measurements. *Geophys J Int*. 2014;199(3):1682–1697. https://doi.org/10.1093/gji/ggu332.

26 Auld BA. *Acoustic Fields and Waves in Solids I, II*. John Wiley & Sons; 1973.

27 Backus G. A geometrical picture of anisotropic elastic tensors. *Rev Geophys*. 1970;8: 633–671. https://doi.org/10.1029/RG008I003P00633.

28 Helbig K. In: Helbig K, ed. *Foundations of Anisotropy for Exploration Seismics*. vol. 22. Pergamon; 1994. Firts.

29 Baerheim R. Harmonic decomposition of the anisotropic elasticity tensor. *Q J Mech Appl Math*. 1993;46(3):391–418. https://doi.org/10.1093/qjmam/46.3.391.

30 Zou WN, Tang CX, Lee WH. Identification of symmetry type of linear elastic stiffness tensor in an arbitrarily orientated coordinate system. *Int J Solid Struct*. 2013;50(14-15):2457–2467. https://doi.org/10.1016/j.ijsolstr.2013.03.037.

31 Aristégui C, Baste S. Localization of the crystallographic directions of composite materials from wavespeed measurements. In: Thompson DO, Chimenti DE, eds. *Review of Progress in Quantitative Nondestructive Evaluation*vol. 16.

32 Cowin SC, Mehrabadi MM. On the identification of material symmetry for anisotropic elastic materials. *Q J Mech Appl Math*. 1987;40(4):451–476. https://doi.org/10.1093/qjmam/40.4.451.

33 Arts RJ. *A Study of General Anisotropic Elasticity in Rocks by Wave Propagation: Theoretical and Experimental Aspects*. 1993. Published online.

34 Arts RJ, Helbig K, Rasolofosaon P. General anisotropic elastic tensor in rocks: approximation, invariants, and particular directions. In: *1991 SEG Annual Meeting*. 1991:1534–1537. https://doi.org/10.1190/1.1888997.

35 Bona A, Bucataru I, Slawinski M. Material symmetries of elasticity tensors. *Q J Mech Appl Math*. 2004;57(4):583–598. https://doi.org/10.1093/qjmam/57.4.583.

36 Diner C, Kochetov M, Slawinski M. On choosing effective symmetry classes for elasticity tensors. *Q J Mech Appl Math*. 2011;64(1):57–74. https://doi.org/10.1093/qjmam/hbq023.

37 Ting TC-T. *Anisotropic Elasticity: Theory and Applications*. New York: Oxford University Press; 1996.

38 Voigt W. *Lehrbuch Der Kristallphysik*. Leipzig, Berlin: B.G. Teubner; 1910.

39 Musgrave MJP. *Crystal Acoustics*. vol. 24. San Francisco: Holden-Day; 1971.

40 Bukovská Z, Soejono I, Vondrovic L, et al. Characterization and 3D visualization of underground research facility for deep geological repository experiments: a case study of underground research facility Bukov, Czech Republic. *Eng Geol*. 2019;259, 105186. https://doi.org/10.1016/j.enggeo.2019.105186.

41 Bukovská Z, Švagera O, Chabr T, et al. Získání dat z hlubokých horizontů dolu Rožná - závěrečná zpráva TT - data acquisition from the deep horizons of the Rožná mine - final report (Technical report SÚRAO č. 464/2020). In: Dobeš P, Násir MM, Knésl I, et al., eds. *Ústav Geoniky, Studentská 1768 , 708 00 Ostrava - Poruba*; 2020. http://www.ugn.cas.cz/. http://www.nusl.cz/ntk/nusl-432165.

42 Berčáková A, Melichar R, Souček K. Mechanical properties and failure patterns of migmatized gneiss with metamorphic foliation under UCS test. *Rock Mech Rock Eng.* 2020;53(4):2007–2013. https://doi.org/10.1007/s00603-019-02012-2.

43 Petružálek M, Lokajíček T, Svitek T, Jechumtálová Z, Kolář P, Šílený J. Fracturing of migmatite monitored by acoustic emission and ultrasonic sounding. *Rock Mech Rock Eng.* 2019;52(1):47–59. https://doi.org/10.1007/s00603-018-1590-2.

44 Wenning QC, Madonna C, de Haller A, Burg J-P. Permeability and seismic velocity anisotropy across a ductile–brittle fault zone in crystalline rock. *Solid Earth.* 2018;9:683–698.

45 Wehrens P, Baumberger R, Berger A, Herwegh M. How is strain localized in a meta-granitoid, mid-crustal basement section? Spatial distribution of deformation in the central Aar massif (Switzerland). *J Struct Geol.* 2016;94:47–67. https://doi.org/10.1016/j.jsg.2016.11.004.

46 Keusen HR, Ganguin J, Schuler P, Buletti M. Grimsel test site: geology. *Geologie.* 1989;21(12):1–167.

47 Nejati M, Dambly MLT, Saar MO. A methodology to determine the elastic properties of anisotropic rocks from a single uniaxial compression test. *J Rock Mech Geotech Eng.* 2019;11(6):1166–1183.

48 Dambly MLT, Nejati M, Vogler D, Saar MO. On the direct measurement of shear moduli in transversely isotropic rocks using the uniaxial compression test. *Int J Rock Mech Min Sci.* 2019;113:220–240. https://doi.org/10.1016/J.IJRMMS.2018.10.025.

49 Pros Z, Babuška V. An apparatus for investigating the elastic anisotropy on spherical rock samples. *Studia Geophys Geod.* 1968;12(2):192–198. https://doi.org/10.1007/BF02587847.

50 Lokajícek T, Svitek T. Laboratory measurement of elastic anisotropy on spherical rock samples by longitudinal and transverse sounding under confining pressure. *Ultrasonics.* 2015;56:294–302.

51 Svitek T, Vavryčuk V, Lokajíček T, Petružálek M, Kern H. Effect of pressure on 3D distribution of P-wave velocity and attenuation in antigorite serpentinite. *Geophysics.* 2017;82(4):1–42. https://doi.org/10.1190/GEO2017-0006.1.

52 Klíma K, Červený V. The computation of the elastic constants of an anisotropic medium from the velocities of body waves. *Studia Geophys Geod.* 1973;17(2):115–122.

53 Svitek T, Rudajev V, Petružálek M. Determination of P – wave arrival time of acoustic events. *Acta Montan Slovaca.* 2010;15(2):145–151.

54 Greenfield RJ, Graham EK. Application of a simple relation for describing wave velocity as a function of pressure in rocks containing microcracks. *J Geophys Res Solid Earth.* 1996;101:5643–5652. https://doi.org/10.1029/95JB03462.

55 Christensen NI. Compressional wave velocities in possible mantle rocks to pressures of 30 kilobars. *J Geophys Res.* 1974;79(2):407–412. https://doi.org/10.1029/JB079i002p00407.

56 Vavryčuk V. Parabolic lines and caustics in homogeneous weakly anisotropic solids. *Geophys J Int.* 2003;152(2):318–334. https://doi.org/10.1046/j.1365-246X.2003.01845.x.

57 Vavryčuk V. Focal mechanisms in anisotropic media. *Geophys J Int.* 2005;161:334–346. https://doi.org/10.1111/j.1365-246X.2005.02585.x.

58 Vavryčuk V. Spatially dependent seismic anisotropy in the Tonga subduction zone: a possible contributor to the complexity of deep earthquakes. *Phys Earth Planet In.* 2006;155(1-2):63–72. https://doi.org/10.1016/j.pepi.2005.10.005.

59 Lokajicek T, Vasin R, Svitek T, et al. Intrinsic elastic anisotropy of westerly granite observed by ultrasound measurements, microstructural investigations, and neutron diffraction. *J Geophys Res Solid Earth.* 2020;126(1):1–23. https://doi.org/10.1029/2020JB020878.

60 Nejati M. *On the Anisotropy of Mechanical Properties in Grimsel Granodiorite.* ETH Zurich; 2018. https://do.

61 Fjær E, Holt RM, Horsrud P, Raaen AM, Risnes R. Chapter 5 elastic wave propagation in rocks. *Developments in Petroleum Science.* 2008;53:175–218.

Further references

62 Simmons G, Wang H. *Single Crystal Elastic Constants and Calculated Aggregate Properties. A Handbook.* second ed. The M.I.T. press; 1971.

63 Rose ME. *Elementary Theory of Angular Momentum.* John Wiley & Sons, Inc.; 1957.